Progenitor cell integration into a barrier epithelium during adult organ turnover

Paola Moreno-Roman[1,†], Yu-Han Su[1], Anthony Galenza[1], Lehi Acosta-Alvarez[1], Alain Debec[2§],Antoine Guichet[2], Jon-Michael Knapp[3], Caroline Kizilyaprak[4], Bruno M. Humbel[4,5,‡], Irina Kolotuev[4], & Lucy Erin O'Brien[1*]

Affiliations:

[1]Department of Molecular & Cellular Physiology, Stanford School of Medicine, Stanford, CA 94305 USA

[2]Equipe Polarité et Morphogenèse, Institut Jacques Monod, CNRS-Université de Paris, 75205 Paris CEDEX 13 – France

[3]Luminint Consulting Group, LLC.

[4]Universite de Lausanne, Bâtiment Biophore, Quartier Sorge, CH-1015 Lausanne, Switzerland

[5]Department of Cell Biology and Neuroscience, Juntendo University Graduate School of Medicine, Tokyo 113-8421, Japan

[†]Present address: Foldscope Instruments, Inc.

[‡]Present address: IMG, Okinawa Institute of Science and Technology, Tancha, Okinawa, Japan

[§]Present address: Institute of Ecology and Environmental Sciences, iEES, Sorbonne University, UPEC, CNRS, IRD, INRA, F-75005 Paris, France

***Corresponding author:** lucye@stanford.edu

ABSTRACT

Barrier epithelial organs face the constant challenge of sealing the interior body from the external environment while simultaneously replacing the cells that contact this environment. These replacement cells—the progeny of basal stem cells—are born without apical, barrier-forming structures such as a protective, lumen-facing membrane and occluding junctions. How stem cell progeny acquire these structures to become part of the barrier is unknown. Here we use Focused Ion Beam-Scanning Electron Microscopy (FIB-SEM), Correlative Light-Electron Microscopy (CLEM), and volumetric imaging of live and fixed organs to investigate progenitor integration in the intestinal epithelium of adult *Drosophila*. We find that stem cell daughters gestate their future lumenal-apical membrane beneath a transient, basal niche formed by an umbrella-shaped occluding junction that shelters the growing cell and adheres it to mature neighbor cells. The umbrella junction both targets formation of a deep, microvilli-lined, apical invagination and closes it off from the contents of the gut lumen. When the growing cell is sufficiently mature, the umbrella junction retracts to expose this Pre-Assembled Apical Compartment (PAAC) to the gut lumen, thus incorporating the new cell into the intestinal barrier. When we block umbrella junctions, stem cell daughters grow and attempt to differentiate but fail to integrate; when we block cell growth, no umbrella junctions form and daughters arrest in early differentiation. Thus, stem cell progeny build new barrier structures in the shelter of a transient niche, where they are protected from lumenal insults until they are prepared to withstand them. By coordinating this dynamic junctional niche with progenitor cell differentiation, a physiologically active epithelial organ incorporates new cells while upholding integrity of its barrier.

INTRODUCTION

Barrier epithelial organs protect the body interior from the external environment while performing physiological processes that require direct exposure to this environment. For example, the epithelium of the digestive tract both protects the body from gastric acid and enteric pathogens while simultaneously breaking down and absorbing ingested nutrients. The dual roles of barrier epithelia create a conundrum: Optimal physiological function requires that the tissue replace old, spent cells with new stem cell progeny, but each individual progeny must be incorporated into the epithelium without compromising barrier integrity (Guillot and Lecuit, 2013; Leblond, 1981; Liang et al., 2017; Macara et al., 2014; Pellettieri and Alvarado, 2007). The cellular mechanisms which enable stem cell progeny to seamlessly assimilate into a functioning barrier are poorly understood.

In all metazoans, epithelial barrier function arises from two conserved features of the epithelial cells themselves. First, cell-cell occluding junctions—tight junctions in vertebrates, septate junctions in invertebrates—create impermeable seals between cells (Varadarajan et al., 2019). Occluding junctions encircle each epithelial cell at the lateral border of the apical membrane, creating a sealed network that prevents even small molecules from freely passing between the lumen and the body interior. Second, a lumen-facing, apical plasma membrane, tightly folded into microvilli or cilia, forms a mucosal shield that resists corrosives, pathogens, and other lumenal insults (Linden et al., 2008; McGuckin et al., 2011; Overeem et al., 2015). This apical membrane is a hallmark of epithelial differentiation and serves as the barrier's direct interface with the outside world. In contrast, the stem cells that renew many barrier epithelia lack occluding junctions and a lumen-contacting apical membrane. Examples of such epithelia include the mammalian trachea (Evans and Moller, 1991; Michael J. Evans, 2001; Rock et al., 2009; Sekiya et al., 1988), mammary gland (Chepko and Dickson, 2003; Chepko and Smith, 1997), prostate (Tsujimura et al., 2002), cornea (Cotsarelis et al., 1989), and olfactory lining (Leung et al., 2007), and the *Drosophila* adult midgut (Korzelius et al., 2014; Resnik-Docampo et al., 2017; Xu et al., 2019). Stem cells in these tissues are much smaller than their mature progeny; they inhabit the basal region of the epithelium, protected from lumenal contents by the mature cells' occluding junction network.

Since stem cells lack barrier-forming structures, their progeny must generate these structures *de novo* as they integrate into the barrier during terminal differentiation. Radial intercalation has been proposed to be this integration mechanism (Walck-Shannon and Hardin, 2014; Sedzinski et al., 2016; Chen et al., 2018). Many developing epithelial tissues use radial intercalation to merge basally derived cells into an overlying epithelium (Merzdorf et al., 1998; Deblandre et al., 1999; Stubbs et al., 2006; Voiculescu et al., 2007; McMahon et al., 2008; Campbell et al., 2010). In this process, a cell that is born basal to the occluding junction network integrates into this network by moving apically while wedging itself between pre-existing cells. When the tip of the intercalating cell reaches the epithelium's occluding junctions, the new cell forms occluding junctions with its neighbors. These SJs begin as a pinpoint and morph into a ring that surrounds the cell's nascent, lumen-facing apical membrane. This apical membrane and its encircling occluding junction expand radially as the cell grows to its final size (Stubbs et al., 2006; Sedzinski et al., 2016, 2017). Similar to these developmental contexts, integration of adult stem cell progeny involves basal-to-apical movement and *de novo* formation of barrier-forming structures. Whether stem cell progeny use radial intercalation or an alternate, perhaps novel, mechanism, remains unexamined.

We leveraged recent advances in Focused Ion Beam-Scanning Electron Microscopy (FIB-SEM), Correlative Light-Electron Microscopy (CLEM – (Burel et al., 2018)), and *in vivo* volumetric confocal live imaging (Martin et al., 2018) to directly examine this question using the midgut of adult *Drosophila*. Like many vertebrate barrier epithelia, the epithelial lining of the fly midgut is a leakproof, pseudostratified epithelium that is continually renewed through the divisions of basal stem cells (Lemaitre and Miguel-Aliaga, 2013). Investigating how new stem cell progeny assimilate

into this adult barrier epithelium, we found—unexpectedly—that assimilation occurs not by radial intercalation but by a striking morphogenetic process that has not previously been described for any tissue.

We discovered that as a stem cell daughter undergoes terminal differentiation, its nascent occluding junctions form a transient, umbrella-shaped niche that supports development of the cell's future, lumen-facing apical surface. This surface starts as an intercellular, localized delamination within the umbrella-shaped junction. The delaminated membrane of the differentiating cell accumulates apical markers, invaginates deeply into the cell's cytoplasm, and folds into microvilli in the shelter of the junctional niche; these behaviors create a pre-assembled apical compartment (PAAC) on the basal side of the epithelial barrier, protected from the contents of the gut lumen. In the final phase of cell differentiation, the umbrella junction retracts to fuse the PAAC with the gut lumen, and the apical membrane everts to form the mature cell's convex lumenal surface.

The morphogenetic process of progenitor cell integration is coupled to growth that progenitor cells undergo as they terminally differentiate. When we block stem cell daughters from integrating, they become trapped in a hybrid, partially differentiated state and accumulate on the basal side of the epithelium. These animals die prematurely, implying that organismal longevity is compromised when the intestinal barrier is not properly replenished.

We suggest that PAAC-mediated integration enables stem cell progeny to generate lumen-facing cell surfaces in a space that is protected from lumenal insults, thus enabling new cells to be added seamlessly to a physiologically active barrier epithelium.

RESULTS

Mature intestinal enterocytes form the bulk of the *Drosophila* midgut and are responsible for its barrier function. Like their vertebrate counterparts, *Drosophila* enterocytes are bonded together by apical occluding junctions (Figs. 1A & 2A). In the fly gut, these occluding junctions are smooth septate junctions (SJs) (Furuse and Izumi, 2017). Also like their vertebrate counterparts, *Drosophila* enterocytes display an apical brush border composed of long, dense microvilli (Fig. 2A); the brush border both absorbs nutrients and protects against lumenal pathogens.

Enterocytes are terminally differentiated and post-mitotic. When shed through damage or death, they are replaced by division of resident stem cells (Micchelli and Perrimon, 2006; Ohlstein and Spradling, 2006; Jiang and Edgar, 2009; Liang et al., 2017). Stem cell progeny that are fated to become enterocytes must first pass through an intermediate, post-mitotic stage called an enteroblast (Ohlstein and Spradling, 2007; Bardin et al., 2010; Perdigoto et al., 2011) (Figure 1A). Enteroblast identity is determined by activation of the Notch receptor and can be visualized using Notch reporters such as *Su(H)-GFP::nls* and *Su(H)-lacZ* (Ohlstein and Spradling, 2007; Bardin et al., 2010; Perdigoto et al., 2011; de Navascués et al., 2012). As enteroblasts differentiate to enterocytes, they endoreplicate from 2N to 32-64N and increase in volume by ~30x (Xiang et al., 2017).

Stem cell progeny initiate new SJs at discrete contact points with mature cells

We were intrigued by prior observations that stem cells lack SJs (Korzelius et al., 2014; Resnik-Docampo et al., 2017; Xu et al., 2019) because this implies that differentiating cells must form SJs *de novo* and integrate themselves into the enterocytes' leakproof SJ network. We sought to determine when, where, and how *de novo* SJ formation occurs. First, we asked whether enteroblasts form SJs with their mature enterocyte neighbors (Figs. 1 & 2). If so, then SJ components should localize to enteroblast-enterocyte interfaces. To investigate this prediction, we used midguts that expressed markers to distinguish enteroblasts, enterocytes, and stem cells. We immunostained them for the SJ components Snakeskin (Ssk) and Tetraspanin2A (Tsp2A) (Yanagihashi et al., 2012; Izumi et al., 2016), then performed 5-channel multi-photon laser scanning microscopy to visualize SJs in the context of identified cells.

We observed SJ components at nearly all enteroblast-enterocyte interfaces, but not at the vast majority of stem cell-enterocyte interfaces nor at any stem cell-enteroblast interfaces. 89% of stem cells (*escargotGAL4, UAS-his2b::CFP* (*esg*$^+$), Armadillo (Arm$^+$), Su(H)-GFP:nls$^-$) exhibited no co-localization with SJ components (n=119 stem cells from 5 guts) (Fig. 1B & 1E), as expected (Korzelius et al., 2014; Resnik-Docampo et al., 2017; Xu et al., 2019). By contrast, 92% of enteroblasts (*esg*$^+$, Arm$^+$, Su(H)-GFP:nls$^+$) (Figs. 1C, 1D, 1F & 1G) overlapped with enterocyte-enterocyte SJs (n=125 enteroblasts from 5 guts). Many SJ-contacting enteroblasts exhibited small, presumably diploid, nuclei, which suggests that these contacts are formed in initial stages of enteroblast fate determination.

Enteroblast SJ staining invariably localized to the apical-most tips (apex) of the enteroblasts, where it overlapped with the basal terminus of the enterocyte SJs. This overlap might represent either *bona fide* adhesion septa between enteroblasts and enterocytes or else the mere physical proximity without formation of true adhesion septa. To distinguish these scenarios, we performed correlative light-electron microscopy (CLEM) (Kolotuev, 2014) on *Su(H)-GFP::nls*-expressing midguts to identify the GFP-labelled enteroblasts. FIB was performed in random positions of the midgut R4c region; GFP-labeled enteroblasts were identified; and interfaces between these enteroblasts and neighbor enterocytes were examined for potential SJ septa.

In EM, SJ septa characteristically appear as electron-dense structures that 'fuse' together the apposing plasma membranes of adjacent cells. As expected, enterocyte-enterocyte septa fused together the apical-most regions of the cells' lateral membranes, directly adjacent to their microvilli-rich brush borders (Fig. 2A). However, when enterocytes were next to an enteroblast (Figs. 2B-2E), their SJs extended basally toward the enteroblast (red pseudocolor in Fig. 2B'') and fused with enteroblast plasma membrane at its apex (arrowheads). These observations demonstrate that enteroblasts form *bona fide* SJ septa with mature neighbor cells. In addition, they imply that light-microscopy visualized overlap of immunostained SJ components with enteroblast cell membranes (Fig. 1) are sites of new SJ formation.

To understand the three-dimensional structure of enteroblast-enterocyte SJs, we performed array tomography. We transformed the tomograms into volumetric renderings of individual cells and their SJ interfaces. Fig. 2C and Video 1 show the volumetric rendering of a 30-slice series surrounding the CLEM image in Fig. 2B. The apex of this diploid (presumably, newly determined) enteroblast (red) exhibits three finger-like projections (arrowheads), each of which forms a point-like, discrete SJ (green) with one of its three neighbor enterocytes (blue; labelled 1-3 in Fig. 2B). No SJs are visible between the enteroblast and an adjacent, Su(H)-GFP:nls-negative stem cell (yellow). The enteroblast's three point-like SJs contact the three enterocyte SJs (pink, pale blue, and purple) at the latters' basal rim. Importantly, we found no discontinuities between the new, enteroblast-enterocyte SJs (overlap between green and either pink, pale blue, or purple) and the pre-existing, enterocyte-enterocyte SJs (overlap between pink and pale blue, pink and purple, or pale blue and purple). This structural continuity suggests that the pre-existing, enterocyte-enterocyte SJ guides the localization of initial SJ contacts between enterocytes and the new enteroblast.

SJ contacts develop into a large, umbrella-shaped SJ that covers the enteroblast apex and extends toward the basal epithelium

We next generated a volumetric rendering of a larger (hence, likely older) enteroblast (red) from a 413-slice FIB-SEM tomographic series that spanned a 35.6μm x 35.6μm x 4.5μm tissue volume. A single slice from this series is shown in Figs. 2D-D'' and Fig. S1, and the volumetric rendering is shown in Figure 2E and Video 2. In contrast to the nascent SJ contacts formed by a young enteroblast (Figures 2B & 2C), the SJ (green) of this older enteroblast is an expansive, adhesive 'zone' whose shape resembles an umbrella. This umbrella SJ fuses the pyramidal enteroblast to three mature neighbor cells: the SJs (pink and purple) of two enterocytes (blue; labelled 1 and 2 in Figs. 2D & 2E) and those of an enteroendocrine cell (pale blue; labelled 3 in Fig. 2D). No SJs are visible at the interface between the enteroblast and a presumptive stem cell (yellow). As with SJs of the young enteroblast (Fig. 2B-C), the SJs between the older enteroblast and its neighbor enterocytes (green/pink overlap and green/purple overlap) are continuous with the SJ that had previously formed between the enterocytes themselves (pink/purple overlap).

Importantly, the umbrella SJ extends unusually far toward the basal epithelium—a feature that is incompatible with a simple model of radial intercalation. SJs typically occupy a narrow band at the apical border of the enterocytes' lateral membranes (Fig. 2A; also in Fig. 2E and E', the purple SJ on left side of enterocyte 1 and pink SJ on right side of enterocyte 2). In radial intercalation, the SJ initiates at the point where the new cell's apical tip becomes co-planar with the organ's mature SJ network; hence, the new SJ grows to a narrow width that matches that of mature SJs (Walck-Shannon and Hardin, 2014; Stubbs et al., 2006; Sedzinski et al., 2016, 2017; Chen et al., 2018). However, an enteroblast's umbrella SJ spreads basally along two-thirds of the enterocytes' lateral membranes and shrouds the top third of the enteroblast (Fig. 2E, green SJ and associated pink and

234 purple SJs; Video 2). This basally-extended umbrella shape implies an alternate mode of integration
235 in which the new SJ forms basal to the organ's mature SJ network.

236 Cloning Meduse, an actin-associated protein that localizes to the brush border of midgut 237 enterocytes

238 The second component of the gut's barrier structure is collectively formed by the apical cell
239 surfaces that line the gut lumen. Mature enterocytes fold these surfaces into long, dense microvilli,
240 forming the intestinal brush border (Fig. 2A). Mature enterocytes also exhibit apical-basal polarity,
241 as characterized by lumen-polarized localization of cytoskeleton-associated proteins such as Moesin,
242 Karst (β_H-spectrin), and Myosin7a (Baumann, 2001; Chen et al., 2018).

243 Another luminally polarized marker is provided by the splice-trap transposon line
244 A142(Bobinnec et al., 2003; Buchon et al., 2013), which expresses a GFP fusion protein that co-
245 localizes with Moesin at or near enterocyte microvilli (Fig. 3A-C). We found that this transposon is
246 inserted into CG2556 (Fig. S2A), a previously uncharacterized gene that does not appear to have
247 vertebrate homologs. Since the filamentous appearance of the A142 fusion protein in egg chambers
248 is reminiscent of sea jelly tentacles (Fig. S2B), we named this gene Meduse (Mdu). Mdu is predicted
249 to be a 470 amino-acid, 51 kDa protein whose sole identifiable motif is an actin binding domain. This
250 putative actin-binding function is consistent with localization of the A142 splice trap to the apical
251 brush border of enterocytes and with actin filaments in Stage 10 egg chambers, the latter of which is
252 latrunculin-sensitive (Fig. S2B-C).

253 The umbrella SJ is a transient niche for formation of the new cell's future lumenal-apical 254 surface

255 During development of tubular epithelial organs, cells generally couple the formation of a
256 lumen-contacting cell surface to the formation of apical features including microvilli, occluding
257 junctions, and apically polarized membrane and cytoskeletal proteins (Blasky et al., 2015; Datta et
258 al., 2011; O'Brien et al., 2002; Sigurbjörnsdóttir et al., 2014). By comparison, stem cells in the adult fly
259 gut lack this entire suite of lumenal-apical features (Figs. 2B-2E) (Chen et al., 2018). How do stem cell
260 progeny generate a lumenal-apical surface as they differentiate, and how do they coordinate apical
261 morphogenesis with SJ formation and epithelial integration?

262 To address this question, we used high-resolution images of fixed guts to identify cells at
263 distinct stages of differentiation, assessed the localization of apical markers, and correlated apical
264 marker localization to SJ maturation (Figs. 3 & S2 and Video 3). Midguts that express Su(H)-lacZ
265 were used because the long perdurance of β-galactosidase (>20 h half-life (Bachmair et al., 1986))
266 makes it possible to identify early-stage enterocytes that have recently turned off enteroblast-specific
267 *Su(H)* activity but have not yet completed terminal morphogenesis (Fig. S3). Comparing apical

marker localization, SJ morphology, and the cytoplasmic and nuclear sizes of Su(H)-lacZ$^+$ cells, we distinguished four stages of apical membrane morphogenesis.

In Stage 1 (left-most column in Fig. 3), enteroblasts are small, and their nuclei appear diploid; this stem-like appearance is consistent with the cells being in early stages of terminal differentiation. Stage 1 enteroblasts lack apical polarity, but they have formed SJ contacts with enterocytes. The few apical markers that are expressed, such as Moesin (Figs. 3A and C), do not show a polarized distribution; other apical markers, such as Karst and Mdu (Figs. 3B and 3C), are not detectable. The apex of Stage 1 enteroblasts contacts the basal terminus of enterocyte-enterocyte SJs, as revealed by localization of SJ components Tsp2A and Ssk (Figs. 3A and 3C). We interpret these SJ contacts to be nascent, point-like SJs, similar to those formed by the enteroblast in Figs. 2B and 2C.

In Stage 2 (Fig 3, second column from left), enteroblasts preferentially localize apical markers to their apex; this enrichment forms a bright plaque that is covered by broadened SJ contacts (Figs. 3A-C). We suggest that this apical plaque represents early stages of polarization since low levels of apical markers persist at other cortical regions. The enteroblast SJ grows to cover the cell's entire apex; we infer that these Stage 2 SJs are similar to the SJ in Figs. 2D and 2E. With respect to morphology, some Stage 2 enteroblasts (e.g. Figs. 3B and 3C) are similar in cytoplasmic and nuclear size to Stage 1 enteroblasts; other Stage 2 enteroblasts are slightly larger, and their nuclei appear intermediate in ploidy between 2N stem cells and 32-64N, mature enterocytes (e.g. Fig. 3A).

In Stage 3 (Fig. 3, third column from left), the differentiating cells resemble immature enterocytes. Their cytoplasmic and nuclear volumes are larger than Stage 1-2 enteroblasts, yet smaller than mature enterocytes, and their low levels of β-galactosidase suggest that Su(H) enhancer activity was diminishing. We refer to these cells as pre-enterocytes. Apical markers—now highly expressed—localize to a conspicuous, concave structure that is covered by the broad, umbrella-shaped SJ sheet that we described above. These concave structures are the morphological hallmarks of Stage 3. With diameters up to 12 μm—roughly the diameter of a mature enterocyte—they often fill the apex of the pre-enterocytes. We were surprised to discover that they are topologically discontinuous with the midgut lumen (Video 3), another feature that is incompatible with radial intercalation. Instead, we conjecture that these structures are precursors of the pre-enterocytes' future lumen-contacting surface. Hence, we designate them as Pre-Assembled Apical Compartments (PAACs).

In Stage 4, (Fig. 3, right column), pre-enterocytes finish integrating into the gut epithelium by acquiring a topology of cell-cell interfaces that is equivalent to mature enterocytes. Stage 4 cells are circumscribed (rather than covered as in previous stages) by SJs, and they now possess a lumen-contacting apical surface. The shapes of Stage 4 lumen-contacting surfaces and Stage 3 PAACs are highly similar, which suggests that the PAAC opens up to the gut lumen via remodeling of its overlying umbrella SJ into a ring. Stage 4 cells are smaller in cytoplasmic volume and nuclear size compared to mature enterocytes. In a final Stage 5 (Fig. S3D), the cell acquires its mature size and

305 ploidy and everts its lumenal-apical surface to form a convex shape, thus completing terminal
306 differentiation.

307 Altogether, this morphogenetic sequence reveals that midgut stem cell progeny do not form
308 new SJs and an apical membrane via radial intercalation into the epithelial barrier. Rather, they form
309 these barrier structures while still in the basal epithelium, protected by the mature barrier.

310 Live imaging of enteroblast-enterocyte integration

311 We next asked whether live imaging corroborates the four-stage sequence (Fig. S3D) of
312 enteroblast-enterocyte integration implied by fixed samples. To address this question, We
313 performed continuous time-lapse imaging using Windowmount methodology, in which volumetric
314 movies of physiologically functioning guts are captured in live animals through a window cut into
315 the dorsal cuticle (Fig. 4A) (Martin et al., 2018). Prior analyses of stem cell clones in both fixed guts
316 (He et al., 2019; de Navascués et al., 2012) and intravital live imaging (Koyama et al., 2020) suggest
317 that most enteroblasts require >24 h to differentiate into enterocytes. Although this time frame is
318 longer than the 16-20 h viability of animals during Windowmount (Martin et al., 2018), longitudinal
319 imaging suggests that some cells differentiate in <24 h (Koyama et al., 2020). Therefore, we aspired
320 to capture these faster cells.

321 We first examined live dynamics of SJs. From nine movies of *GS5966>tsp2A::GFP; Su(H)-*
322 *mCherry* midguts with durations from 7.25-20 h, we identified one movie in which an mCherry-
323 expressing cell increased in cross-sectional area by nearly three-fold (Fig. 4B & 4D, and Video 4); this
324 dramatic growth is an identifying feature of enteroblast-enterocyte differentiation. To determine
325 whether the Tsp2A::GFP-labelled SJ associated with this cell exhibited dynamics consistent with the
326 mechanism implied by Fig. 3, we analyzed an orthogonal view through the cell's apical-basal axis
327 (Fig. 4C). In the movie's initial 105 min, the SJ that contacted the differentiating cell grew broader
328 and ultimately covered the cell's entire apex (Fig. 4C, arrow in 0- and 90-min panels; Video 4, 0-105
329 min). This broadening is consistent with the notion that SJs expand from discrete contact points in
330 Stage 1 (Fig. 2C, Fig. 3A & 3B, and Video 1) to an umbrella shape in Stages 2 and 3 (Fig. 2E, Video 2,
331 Fig. 3A & B, Fig. 5D, and Video 6). Between 120-285 min, a hollow space developed along the SJ's
332 apical-basal axis; simultaneously, the SJ extended along the lateral faces of the now-larger cell (Fig.
333 4C, arrows (SJ) and asterisks (hollowing) in 195- and 285-min panels; Video 4, 120-285 min). This
334 hollowing and lateral extension are consistent with remodeling of the SJ from an overlying sheet in
335 Stage 3 to a circumscribing ring in Stage 4 (Fig. 3A & 3B). Overall, these live SJ dynamics support the
336 morphogenetic sequence suggested by the fixed analyses in Fig. 3.

337 We next examined live dynamics of the apical membrane using midguts that expressed the
338 apical marker Moesin::GFP and the nuclear marker His2av::mRFP (Fig. 4E and Video 5). The
339 Moesin::GFP-labelled lumenal-apical membranes appeared as a convoluted surface atop the gut
340 cells' nuclei because the apical surface of mature enterocyte is domed (*e.g.* Fig. 2A). Basal to the

lumenal-apical membranes, we frequently observed GFP-labelled structures that were fainter in intensity and concave in shape. We conjecture that these structures are PAACs. While most PAACs did not dramatically change in shape or size during imaging, some PAACs became brighter and deeper over time (*e.g.*, Fig. 4E and Video 5). This evolution is consistent with Stages 3-4 of differentiation, during which PAACs initially form and subsequently become larger and more enriched for apical markers (Fig. 3, Stages 2-3). Overall, we conclude that live imaging of SJ and apical membrane dynamics provides additional support for the four-stage mechanism suggested by fixed tissues.

PAACs are intercellular lumens formed by asymmetric pre-enterocyte apical membranes and enterocyte basolateral membranes

Our finding that PAACs are physically distinct from the gut's lumenal-apical surface raises basic questions about the nature of these structures: Are they intracellular or intercellular? What is their relationship to the developing SJ? Does their apical polarity correspond to a mature brush border? To gain insight into these and other questions, we examined the PAACs' ultrastructure in FIB-SEM tomographic series.

To identify putative PAACs, we first identified pre-enterocytes by looking for polyploid cells that lacked a visible lumenal-apical surface. We noticed that the apexes of such pre-enterocytes frequently contained membrane-bound, ellipsoid ultrastructures (Fig. 5A–cyan box, and Fig. 5B) whose shape and cellular position resembled PAACs. These structures enclosed prominent lumens that are distinct from the gut lumen, circumscribed by SJs, and lined with microvilli. The microvilli are densely arrayed, similar to brush border microvilli, but they are shorter, which suggests they are immature. Notably, Moesin, which outlines PAACs in confocal micrographs (Fig. 3 and Video 3), is a marker of microvilli in other Drosophila epithelia (Edwards et al., 1997; Lattner et al., 2019). We also found sausage-shaped (allantoid) ultrastructures that, like the ellipsoids, are lined with dense microvilli and circumscribed by SJs (Fig. 5A–magenta box, and Fig. 5C). The allantoids' lumens are extremely slender, suggesting that they may be newly formed. Given these features, we conjecture that the ellipsoid ultrastructures are PAACs and the allantoid ultrastructures are their precursors.

We took advantage of our FIB-SEM series to investigate whether PAACs are intracellular compartments that develop within a pre-enterocyte, akin to the large apical endosomes (vacuolar apical compartments/apicosomes) observed in mammalian cells (Gilbert and Rodriguez-Boulan, 1991; Taniguchi et al., 2017; Vega-Salas, 1988) or intercellular compartments that develop between a pre-enterocyte and its mature enterocyte neighbors. We selected series that captured the near-complete volume of individual PAACs or PAAC precursors, and we analyzed their membrane topologies slice-by-slice (Figs. 5B and 5C). We also generated a volumetric rendering of a 200-slice FIB-SEM tomographic series that contained a PAAC, a PAAC precursor, and their associated pre-enterocyte within a tissue volume of 40.2 μm x 23.9 μm x 8 μm (Fig. 5D and Video 6).

These analyses invariably uncovered a region in which pre-enterocyte and mature enterocyte membranes separate from each other to form the PAAC's lumenal space (Fig. 5B and Video 6). Thus, PAACs are intercellular. The PAAC lumen is surrounded by an expansive SJ that adheres the pre-enterocyte to mature enterocytes; this SJ separates the PAAC from the gut's central lumen. The ultrastructure of the PAAC-associated SJ is consistent with the SJs we observed in immunostained, Stage 3 pre-enterocytes (Fig. 3 and Video 3). PAAC precursors—even very small ones—also comprise an intercellular lumen surrounded by an expansive SJ. We did not observe any microvilli-lined compartments that were entirely intracellular. The similar topology of PAACs and PAAC precursors suggests that PAACs initiate via de-adhesion of apposing plasma membranes rather than fusion of an intracellular compartment with the SJ.

PAACs' split apical/basolateral polarity is unique for a lumen-encompassing structure

PAAC-forming pre- and mature enterocytes make markedly unequal contributions to the PAAC's overall morphology. The pre-enterocyte plasma membrane represents the vast majority of a PAAC's total surface area. It folds inward at nearly 180 degrees (arrow in Fig. 5B) to create a deep invagination into the pre-enterocyte cytoplasm. This invagination accounts for most of the PAAC's lumenal volume and evokes a scenario in which PAAC development is driven by inward folding of the pre-enterocyte plasma membrane. In contrast to the structured folds of the pre-enterocyte membrane, the mature enterocyte membranes are amorphous and rest like a blobby lid atop the PAAC lumen (Fig. 5B). These differences are even more extreme in PAAC precursors (Fig. 5C).

The contrast between the structured pre-enterocyte membrane and the amorphous enterocyte membrane corresponds to a second—unprecedented—asymmetry of PAACs: their lumenal polarity is split. The PAAC's pre-enterocyte membrane is apical while the partner enterocyte membrane(s), which lacks apical markers (Video 3) and microvilli (Figs. 5B & 5C, and Video 6), is by default basolateral. To our knowledge, this combination has not previously been reported for any epithelial lumen either in cell culture or *in vivo*. Rather, epithelial lumens to date have been either uniformly apical (Blasky et al., 2015; Datta et al., 2011; O'Brien et al., 2002), or, in some rare, experimentally induced cases, uniformly basolateral (Lowery et al., 2009; Wang et al., 1990). However, these prior studies examined lumens that form between cells at similar differentiation states; we conjecture that the PAACs' unique asymmetries derive from their origin between cells at distinct differentiation states.

Enteroblasts must form SJs to integrate and mature into enterocytes

Our data reveal that as stem cell daughters differentiate, they initiate epithelial integration by forming new, sheet-like SJs with mature neighbor cells. What happens when SJ formation is blocked? To examine this question, we generated "SJ-less" enteroblasts and assessed their ability to integrate and differentiate. We inhibited expression of the SJ component *ssk* specifically in enteroblasts by using the enteroblast driver *Su(H)-GAL4* to express a *UAS-sskRNAi* transgene under

control of temperature-sensitive *GAL80*^{ts} (McGuire et al., 2003) (genotype henceforth referred to as *Su(H)*^{ts}*>sskRNAi*). A *UAS-GFP* transgene was also included to identify the RNAi-expressing cells. The *sskRNAi* hairpin was expressed from days 0-4 of adult life, after which midguts were harvested and analyzed. To confirm that *sskRNAi* prevented SJ formation, we performed immunostaining for another SJ component, Coracle. Whereas Coracle localized to the apex of *Su(H)*^{ts}-expressing control cells, it localized to the cytoplasm of *Su(H)*^{ts}*>sskRNAi* cells (Figs. 6A & 6B). This redistribution implies that *sskRNAi* expression prevents proper formation of SJs.

Su(H)^{ts}*>sskRNAi* cells categorically failed to integrate into the gut epithelium. Instead of reaching the gut's central lumen, these cells accumulated beneath the gut's SJ network (Figs. 6A & 6B). Although this basal localization is typical of enteroblasts, *Su(H)*^{ts}*>sskRNAi* cells did not arrest in an enteroblast state. Rather, they grew in volume and endoreplicated their nuclei (Fig. 6C and Figs. S5A & S5B), two behaviors characteristic of pre-enterocytes (Fig. 3, Stages 3 & 4). Yet unlike pre-enterocytes, *Su(H)*^{ts}*>sskRNAi* cells did not adopt a cuboidal or columnar shape and instead became blob-shaped. Similar behaviors were exhibited by MARCM-generated stem cell clones (Lee and Luo, 1999) that were genetically null for SJ components *tsp2A* (Chen et al., 2018) and *mesh* (Fig. S5E & S5F). Thus even as SJ-less cells achieve mature size, they do not become part of the epithelium.

The indeterminate morphology of *Su(H)*^{ts}*>sskRNAi* cells was accompanied by inappropriate, mixed expression of fate-specific transcription factors. Whereas the stem cell/enteroblast transcription factor Sox100B (Doupé et al., 2018; Jin et al., 2020; Meng et al., 2020) was expressed by both control *Su(H)* and *Su(H)*^{ts}*>sskRNAi* cells (Figs. S5A & S5B), the enterocyte transcription factor Pdm1 (Dantoft et al., 2013; Korzelius et al., 2014; Lee et al., 2009) was absent from control *Su(H)* cells yet expressed in *Su(H)*^{ts}*>sskRNAi* cells (Figs. S5C & S5D). Similar, mixed patterns of marker expression were observed by Xu and colleagues upon enteroblast-specific depletion of the SJ component *tsp2A* (Xu et al., 2019).

Altogether, these findings imply that SJ-less cells become trapped in an abnormal, hybrid cellular state in which the distinct features of enteroblasts and enterocytes co-exist abnormally.

Cell growth is required for integration, independent of SJs

Having found that growth is not sufficient for cells to integrate, we asked whether integration requires cell growth. Cell growth during the enteroblast-enterocyte transition is controlled by the Tsc/Rheb/Tor pathway (Amcheslavsky et al., 2011; Kapuria et al., 2012; Nie et al., 2015; Quan et al., 2013; Xiang et al., 2017). Tor pathway activation in enteroblasts can be visualized by immunostaining for the phosphorylated isoform of the Tor kinase substrate eIF4E Binding Protein (phospho-4EBP) (Kapuria et al., 2012). When Tor is inactivated via overexpression of its inhibitor, Tsc1/2, 4EBP is not phosphorylated (Fig. 6F) and differentiation-associated growth is blocked (Kapuria et al., 2012).

We found that growth of SJ-less cells, like growth of normal enteroblasts, depends on Tor. Phospho-4EBP immunostaining showed that *Su(H)^{ts}>sskRNAi* cells are Tor-activated, akin to *Su(H)* control cells (Figs. 6D & 6E). When we conditionally overexpressed *tsc1/2* in either control cells (*Su(H)^{ts}>tsc1/2*) or *ssk* knockdown cells (*Su(H)^{ts}>sskRNAi, tsc1/2*), we abrogated phospho-4EBP and inhibited cell growth (Figs. 6F & 6G).

We next examined whether Tor inactivation and consequent growth inhibition affects the ability of cells to integrate. We assessed SJ formation in *Su(H)^{ts}>tsc1/2* cells by immunostaining guts for Ssk and the *Su(H)-lacZ* reporter and determining whether the Ssk signal contacted the apex of β-galactosidase-labelled cells. Whereas 92% of control *Su(H)* cells formed SJs, only 53% of *Su(H)^{ts}>tsc1/2* cells did (Fig. 6H). Revealingly, no *Su(H)^{ts}>tsc1/2* cells progressed beyond Stage 1 (Fig. 6I). Thus, SJ initiation is not sufficient for integration to progress; enteroblast growth is also necessary. While the precise contribution of growth is currently unclear, it may fuel expansion of the umbrella SJ or to initiate PAAC formation.

Organ-scale impacts of blocked cellular integration

Organ renewal requires that new cells integrate successfully into the epithelium. When cell integration is blocked, what are consequences to organ-scale cellular equilibrium? We first asked whether blocking integration causes undifferentiated cells to accumulate abnormally in the tissue (Fig. 7A). When animals are maintained under stable, *ad libitum* conditions, Su(H)$^+$ cells typically comprise ~10% of total cells in the midgut R4 region (Bonfini et al., 2021; O'Brien et al., 2011; Viitanen et al., 2021). This proportion essentially doubled when we blocked integration by inhibiting new SJ formation (19.1% ± 5.5% of total cells in *Su(H)^{ts}>sskRNAi* guts; 9.3% ± 2.8% in control guts). By comparison, the proportion of Su(H)$^+$ cells remained nearly normal when we blocked integration by inhibiting cell growth (12.0 ± 2.8% in *Su(H)^{ts}>tsc1/2* guts). Concomitant inhibition of both SJ formation and cell growth resembled growth inhibition alone (12.0 ± 3.2% of total cells in *Su(H)^{ts}>sskRNAi, tsc1/2*guts were Su(H)-lacZ$^+$). Thus, whether integration-blocked cells accumulate in the tissue depends on the means through which integration was blocked. One possible reason may be differences in differentiation state of the integration-blocked cells. Early-stage enteroblasts, which still adhere strongly to their mother stem cell, can repress subsequent mother cell divisions (Choi et al., 2011), and Tsc1/2 overexpression—but not SJ inhibition—arrests differentiation at an early stage ((Kapuria et al., 2012) and Figs. 6C & S5C-G). This early-stage arrest may enable growth-inhibited cells to repress production of additional daughter cells.

We next examined whether blocking integration alters the organ's total number of cells (Fig 7B). Comprehensive counts of DAPI-labeled nuclei in the midgut R4ab region revealed that total cell number remains normal when new cells cannot integrate, even for guts in which integration-blocked cells accumulate abnormally (1997 ± 489 cells in control *Su(H)^{ts}* guts compared 1960 ± 398, 2067 ± 210 cells, and 1611 ± 299 cells in *Su(H)^{ts}>sskRNAi*, *Su(H)^{ts}>tsc1/2*, and *Su(H)^{ts}>sskRNAi, tsc1/2*

484 guts, respectively). We speculate that feedback mechanisms inherent to organ-scale control of total
485 cell number (Akagi et al., 2018; Jin et al., 2017; Liang et al., 2017) 'sense' unintegrated cells and exert
486 a compensatory effect on cellular equilibrium.

487 DISCUSSION

488 Epithelial organs maintain a leakproof barrier between the interior body and the external
489 environment even while continuously replacing the cells that directly contact this environment. In
490 many barrier epithelia, these replacement cells derive from basal stem cells and are born without a
491 lumenal-apical surface or occluding junctions, two structures that are essential for barrier integrity.
492 Consequently, daughters must generate these structures *de novo* and integrate into the barrier as
493 they differentiate.

494 We examined this process at ultra-fine spatial resolution during physiological turnover of
495 the *Drosophila* intestinal epithelium. Our analyses led to a previously undescribed mechanism that
496 we term PAAC-mediated integration (Fig. 7C): The new cell forms a broad, umbrella-shaped SJ that
497 serves as a transient niche for biogenesis of the cell's future lumenal-apical surface (the PAAC).
498 When the new cell is sufficiently mature, the umbrella SJ retracts and the PAAC lumen fuses with
499 the gut lumen, exposing the cell's apical membrane to the external environment. In contrast to a
500 prior model of radial intercalation (Fig. 7C), PAAC-mediated integration enables stem cell daughters
501 to form barrier structures in a space sheltered from the contents of the gut lumen—a potentially
502 crucial safeguard for an epithelium that is simultaneously physiologically active and continuously
503 renewing.

504 PAAC architecture: Implications for epithelial lumen formation

505 Lumens are defining features of epithelial tubes, and the molecular and cellular events that
506 drive lumen formation are a topic of intense interest. Our current understanding of lumen formation
507 comes from studying epithelial cells that are at similar states of differentiation (Blasky et al., 2015;
508 Datta et al., 2011; Overeem et al., 2015; Sigurbjörnsdóttir et al., 2014). PAACs provide a first, fine-
509 grained example of how lumens form between cells that are at disparate states of differentiation.
510 This fate difference likely underlies the PAACs' two distinctive characteristics, structural asymmetry
511 and split polarity. Below, we speculate how these PAAC-specific characteristics may shed new light
512 on lumen-forming mechanisms in general.

513 PAACs are, to the extent we can determine, the first type of intercellular lumen that exhibits
514 split polarity—the membranes that form PAACs alternate between apical identity (the pre-
515 enterocyte) and basolateral identity (mature enterocytes) (Figs. 3, 5 & 7C; and Video 6). By
516 comparison, all epithelial lumens of which we are aware are normally enclosed by membranes that
517 are exclusively apical (Blasky et al., 2015; Datta et al., 2011; Overeem et al., 2015; Sigurbjörnsdóttir et
518 al., 2014). Our finding that PAACs' mature enterocyte membranes do not form a secondary apical

519 domain is surprising because cells that contact multiple lumens in developing epithelia form a
520 corresponding apical domain for each lumen (Alvers et al., 2014; Bagnat et al., 2007; Bryant et al.,
521 2010). One possible explanation is that terminally differentiated epithelial cells actively repress
522 secondary apical domains whereas epithelial cells in developmental contexts do not. Another, non-
523 exclusive, possibility is that all lumens transiently exhibit split apical/basal polarity at their earliest
524 stage—one lumen-forming cell initiates an apical domain prior to the others—but that this stage is,
525 in most cases, extremely short-lived, so it has not been detected previously.

526 PAACs' second striking feature is their extreme structural asymmetry: pre- and mature
527 enterocyte membranes, despite being bonded at their edges by the same SJ, acquire shapes that are
528 extreme opposites. The pre-enterocyte PAAC membrane, which grows dramatically and invaginates
529 deeply into the cytoplasm of the differentiating cell, convolutes into sharp folds and broad curves.
530 This structure, which is superimposed onto the membrane's fine-scale microvillar folds, sets the
531 volume of the PAAC. The mature enterocyte membranes, by contrast, appear largely passive. They
532 sit like a lid atop the neck of the pre-enterocyte invagination and do not appear to morph or expand
533 during differentiation (*e.g.,* compare the nascent and advanced PAACs in Fig. 5 and Video 6).

534 These two features, split apical/basolateral polarity and structural asymmetry, provide
535 insight into opposing models of lumen formation. The structural asymmetry of PAACs is
536 incompatible with the prevailing model of lumen formation, in which hydrostatic pressure drives
537 lumen growth (Chan et al., 2019; Dasgupta et al., 2018; Dumortier et al., 2019; Ruiz-Herrero et al.,
538 2017; Yang et al., 2021), because lumens generated by hydrostatic pressure are uniformly convex
539 (Vasquez et al., 2021). Rather, this asymmetry evokes a recently proposed alternative mechanism in
540 which expansion of apical membrane surface drives lumen growth in a pressure-independent
541 manner (Vasquez et al., 2021). Indeed, since growth of the PAAC lumen is accounted for by apical
542 surface expansion of a single cell, PAACs may provide an informative case study of apical surface-
543 driven growth. Identifying the molecular signals that target and stabilize new PAACs will aid in
544 exploring these scenarios.

545 A trade-off between barrier integrity and junction-forming efficiency

546 In both PAAC-mediated integration and radial intercalation, single cells assimilate into an
547 epithelium through basal-to-apical movement. Why do distinct mechanisms exist to reach the same
548 cellular endpoint? We speculate that, in general, basal-to-apical assimilation requires a trade-off
549 between integration speed and barrier integrity. A given mechanism may favor one of these
550 qualities at the expense of the other. In principle, a spectrum of mechanisms enables tissues to
551 employ the mechanism that is best suited to their specific biological context.

552 In this schema, radial intercalation is rapid and parsimonious. It occurs over time scales of
553 minutes or a few hours. New junctions initiate within the pre-existing junctional network and
554 expand directly into their final morphology, an apico-lateral band. Intriguingly, all examples of

radial intercalation described in the literature take place in developing epithelia (Merzdorf et al., 1998; Deblandre et al., 1999; Stubbs et al., 2006; Voiculescu et al., 2007; McMahon et al., 2008; Campbell et al., 2010). Because embryos themselves are housed in a protective environment (such as an egg or a womb), cells in embryonic tissues can display immature junctions and incipient microvilli at the organ's apical surface without risking exposure to the external environment.

PAAC-mediated integration is slower and, since it involves building and then retracting a temporary scaffold, likely less efficient. We estimate that typical time frames for PAAC-mediated integration are >24 h, based on changes in nuclear size of stem cell daughters over time (Koyama et al., 2020). (Indeed, this >24 h time frame presented a challenge for Windowmount live imaging, which typically yields movies ~8-20 h in duration.) A differentiating cell may require this time to construct the umbrella SJ and microvilli-lined PAAC—large structures that will undergo extensive remodeling in subsequent stages. The indirect, more complex nature of PAAC-mediated integration provides an additional layer of protection for differentiating cells—a potentially worthwhile tradeoff for a functionally active organ that continuously processes substances from the external environment.

How do SJs guide differentiating cells into the epithelial sheet? One appealing notion is that they exert myosin-based pulling forces that draw differentiating cells toward the lumen (Varadarajan et al., 2019; Yu and Zallen, 2020). We were, however, unable to identify any impact on integration following enteroblast-specific inhibition of Rho kinase (Rok; data not shown). Since Rok is an essential activator of myosin contractility, this finding implies that myosin-based forces are not required in the integrating cell. A second possibility is that myosin-based pulling forces, or some other cytoskeletal regulator, is required in mature neighbor cells to aid the basal-to-apical movement of differentiating cells. Since SJs bond together mature and differentiating cells, they are well-positioned to coordinate these two cell types during integration. Finally, SJs may serve to polarize growth and/or cytoskeletal assembly along the apical-basal axis of the differentiating cell (Madara, 1987).

Diverse epithelial architectures may use a diversity of cell assimilation mechanisms

Numerous barrier epithelia, including mammalian trachea, cornea, and olfactory lining, have a cellular organization similar to the fly gut (Chepko and Dickson, 2003; Chepko and Smith, 1997; Cotsarelis et al., 1989; Evans and Moller, 1991; Leung et al., 2007; Michael J. Evans, 2001; Rock et al., 2009; Sekiya et al., 1988; Tsujimura et al., 2002). All these tissues are renewed by basally localized stem cells that lack occluding junctions and lumenal-apical surfaces. Their daughter cells thus all face the same architectural challenge of integrating seamlessly into the barrier while they differentiate. Whether they overcome this challenge through PAAC-mediated integration, like the fly gut, or through some other, perhaps as-yet-undefined, mechanism will be an interesting question for future investigation.

In considering how epithelial architecture affects new cell integration, it is notable that two of the best-understood barrier epithelia, mammalian intestine and lung alveoli, sidestep the challenge of barrier integration entirely. In these tissues, stem cells possess both occluding junctions and lumenal-apical surfaces, and daughter cells symmetrically inherit these structures from their mother (Fig. 7C) (DeMaio et al., 2009; Fleming et al., 2007; Jinguji and Ishikawa, 1992; McKinley et al., 2018). Symmetric inheritance is morphogenetically parsimonious, but it requires the abscission of existing junctional septa and creation of new septa at the new daughter-daughter interface. Since this remodeling happens at the lumenal surface, it might produce potential weak points in the barrier. Thus, at first glance, the fact that mammalian intestine and lung use symmetric inheritance to assimilate new cells seems at odds with the idea that physiologically active epithelia need extra safeguards to protect barrier integrity.

We speculate, however, that this potential risk is mitigated by these tissues' particular architecture; namely, deeply recessed niches—intestinal crypts and terminal alveolar endbuds—in which the lumen-exposed stem cells reside. Crypts and endbuds are secluded from bulk lumenal flow, which provides their resident stem cells with built-in protection that stem cells in other epithelia lack. This built-in protection conceivably affords stem cell daughters the simplicity of directly inheriting barrier structures from their mother cell. In this light, PAACs may be seen as a cellular-scale solution for epithelia that lack recessed stem cell niches, the tissue-scale solution for protecting new cells. As such, our findings spotlight the intimate relationship between physiological function, organ form, and cellular differentiation and morphogenesis.

612 **MATERIALS and METHODS**

613 **Drosophila husbandry**

614 Mated adult female flies were used in all experiments. Crosses utilizing the TARGET system
615 (GAL4/GAL80^{ts}) were performed at 18°C (McGuire et al., 2003). Upon eclosion, adult animals were
616 temperature shifted to 29°C for 4 days to inactivate GAL80^{ts} and induce GAL4-mediated expression.
617 Midguts were harvested for immunostaining 4 days after induction. Flies used for
618 immunofluorescence were raised on standard molasses medium at 18°C. Upon eclosion, they were
619 shifted to 29°C. Midguts were harvested for immunostaining 4 days after eclosion.

620 **Immunohistochemistry and sample preparation for confocal microscopy**

621 Dissected guts were fixed in 4% formaldehyde in PBS (pH 7.4) at room temperature for 1
622 hour, immunostained, and mounted as previously described (O'Brien et al., 2011). Primary
623 antibodies: mouse anti-Armadillo (1:100, DSHB N2 7A1), rabbit anti-Snakeskin (1:1000, gift from
624 Furuse lab), mouse anti-Coracle (1:50, DSHB C615.16), mouse anti-β-galactosidase (1:400, Promega
625 Z3781), rabbit anti-Phospho4EBP1 (1:500, Cell Signaling). Secondary antibodies: donkey anti-rabbit
626 IgG conjugated to Alexa 555 and donkey anti-mouse IgG conjugated to Alexa 647 (1:1000, Invitrogen
627 A-31572 and A-31571, respectively). Nuclei were stained with DAPI (LifeTechnologies D1306).
628 Samples were incubated with primary antibody overnight at 4ºC in PBT (PBS with 3% Triton X-100
629 (Sigma-Aldrich X100-100 mL)) with 5% NGS (Capralogics GS0250), washed 3 times in PBT, then
630 incubated with secondary antibody for 4 hours at room temperature in PBT with 5% NGS. Samples
631 were mounted in ProLong (LifeTechnologies P36984) and stored at -20ºC until imaging.

632 **Induction of MARCM clones**

633 Heat-shock MARCM clones (Lee and Luo, 1999) were generated by collecting adult flies 12-
634 24 hours post-eclosion and performing two 45-min, 37ºC heat shocks separated by a 8-min chill on
635 ice. Flies were returned to 25ºC for 4 days, then dissected and analysed.

636 **Fixed sample imaging**

637 Fixed samples were imaged on a Leica SP8 WLL confocal microscope with a 63x HC PL APO
638 CS2 oil objective. Serial optical sections were taken at 0.5 μm intervals through the entirety of whole-
639 mounted, immunostained midguts.

640 **Quantitation of SJ-contacting and non-contacting cells**

641 Enteroblasts in the midgut R4ab region (also known as P1/2) (Buchon et al., 2013; Marianes
642 and Spradling, 2013; O'Brien, 2013) were visualized and counted using ImageJ/Fiji (Schindelin et al.,
643 2012). The R4ab region was identified using morphological landmarks. SJs were identified by
644 immunostaining for the SJ component Snakeskin. Su(H)-lacZ^{+} (β-Gal^{+}) cells were recognized as
645 enteroblasts by visual inspection. To categorize enteroblasts as SJ-contacting or non-contacting, each
646 enteroblast was analyzed through Fiji Orthogonal View. Enteroblasts were defined as SJ-contacting
647 cells if the β-Gal^{+} signal was juxtaposed and/or displayed overlap with apical Snakeskin signal in
648 XY, XZ and YZ planes. Enteroblasts were defined as SJ non-contacting cells if they lacked these
649 criteria.

650 **Measurements of cell volume**

651 To measure volumes of *Su(H)-lacZ*$^+$ cells, tissues were fixed, immunostained using anti-β-
652 galactosidase antibody, mounted, and subjected to volumetric confocal imaging. After initial
653 processing in Fiji, files were imported to Bitplane Imaris v.8.7. Volumes of *Su(H)-lacZ*$^+$ cells were
654 determined by creating a surface for each cell using the Imaris contour tool and then measuring the
655 enclosed volume.

656 **Ovary dissection and staining**

657 Egg chambers were dissected in phosphate-buffered saline (PBS pH 7.4) + 0.1% Triton X-100
658 and incubated for 2 hours in 1mM latrunculin B (LatB; Sigma). They were then fixed 20 min in 4%
659 PFA (in PBS pH 7.4), incubated 2 hours in a 1:250 dilution of TRITC-conjugated phalloidin
660 (Molecular Probes, Eugene, OR), and subsequently imaged on a Zeiss LSM 700 confocal microscope.

661 **Total cell and total enteroblast counts**

662 To perform total cell counts and total enteroblast counts of R4ab, confocal image stacks were
663 digitally isolated in Fiji. Bitplane Imaris was used generate three-dimensional organ reconstructions,
664 and individual cells were comprehensively counted by mapping signals for DAPI (for total cell
665 counts) or Su(H)-lacZ (for total enteroblast counts) to Imaris surface objects. Imaris-recognized
666 surfaces were confirmed through visual inspection and manually adjusted when needed for
667 accuracy.

668 ***In vivo* live imaging and movie analyses**

669 Live imaging was performed on 2-3 day old adult females as described previously (Martin et
670 al., 2018), with the following modifications: For Video 4, 20 nM RU486 and 10 μg/mL Isradipine
671 were added to the imaging media to induce GeneSwitch5966 expression and reduce intestinal
672 peristalsis, respectively. For Video 5, 10 μg/mL Isradipine was added to the imaging media to
673 reduce intestinal peristalsis.

674 Videos were acquired with a LSM Leica SP5 with a HCX APO L 20x/ 1.00W lens, controlled
675 by LAS AF software. Confocal sections were taken every 15 mins with z-steps of 1.01μm (Video 4)
676 and 2.98 μm (Video 5). Videos were processed on a Windows computer (Windows 10 Education)
677 with a 3.70 GHz quad-core Intel Xeon processor and 256 GB memory. Videos were initially
678 processed in Fiji and subsequently visualized in volumetric format and analyzed in Bitplane Imaris.
679 For Video 4, the following Fiji plugins were applied: 1) Stack Sorter
680 (https://www.optinav.info/Stack-Sorter.htm), to correct the alignment of out-of-order slices
681 captured during a peristaltic contraction, 2) StackReg (Arganda-Carreras et al., 2006) to correct for
682 whole-organ X-Y movements, 3) Correct 3D Drift (Parslow et al., 2014) to correct for global volume
683 movements, and 4) TrakEM2 (Cardona et al., 2012) to perform manual X-Y alignment for slices that
684 could not be registered automatically. The latter 3 plugins were applied iteratively as needed. For
685 Video 5, Stack Sorter, StackRed, and Correct 3D Drift were used. The latter two plugins were
686 applied iteratively as needed.

687 **Measurements of cross-sectional cell area in live movies**

688 The cross-sectional area of the integrating Su(H)-mCherry$^+$ cell at each timepoint in Video 4
689 was determined as follows: The cell's largest cross-sectional plane at each time point was identified

by visual inspection. FIJI Measure was used to manually outline the mCherry signal in this plane and to measure the enclosed area.

Sample preparation for FIB-SEM

Fly guts were dissected in PBS and immediately processed as previously described (Daniel et al., 2018; Kolotuev, 2014). Briefly, the samples were fixed in 1% formaldehyde, 2.5% glutaraldehyde in 0.1M phosphate buffer (PB) for 2 hours at room temperature, then incubated for 1 hour in 2% (wt/vol) osmium tetroxide and 1.5% (wt/vol) K4[Fe(CN)6] in PB followed by 1 hour in 1% (wt/vol) tannic acid in 100 mM cacodylate buffer, then 30 minutes in 2% (wt/vol) osmium tetroxide in water followed by 1% (wt/vol) uranyl acetate for 2 hours at room temperature. After the dehydration cycles, samples were embedded in Epon-Araldite mix. Samples were flat embedded to assure the targeting of the region of Interest during the sectioning step.

Sample preparation for CLEM

To preserve native fluorescence for correlative light/electron microscopy, samples were subjected to high-pressure freezing followed by rapid freeze-substitution, as previously described (Kolotuev, 2014; Kolotuev et al., 2010). Dissected guts were immediately transferred to large high pressure freezing carriers filled with 20% bovine serum albumin for cryo-protection and frozen using the standard procedure according to the manufacturer's instructions (High Pressure Freezing Machine HPF Compact 02, Engineering Office M. Wohlwend GmbH, Sennwald, Switzerland). Samples were substituted in an AFS2 machine (Leica) with 0.1% uranyl acetate diluted in anhydrous acetone and embedded in HM20 acrylic resin mix (Electron Microscopy Sciences). To assure precise orientation of the samples, the flat embedding procedure was used (Kolotuev, 2014).

Electron microscopy image acquisition and analysis

Polymerized flat blocks were trimmed using a 90° diamond trim tool (Diatome, Biel, Switzerland) mounted on a Leica UC6 microtome. Transmission electron microscopy samples were analyzed with an FEI CM100 electron microscope operated at 80kV, equipped with a TVIPS camera piloted by the EMTVIPS program.

Samples for CLEM were sectioned at 100-150 nm thickness and transferred to wafers using an array tomography protocol (Burel et al., 2018; Kolotuev and Micheva, 2019). CLEM wafers were first imaged for fluorescence signal using a Zeiss fluorescent microscope equipped with DAPI and GFP filters using 20x and 60x objectives. To analyze the ultrastructure, sections on wafer were contrasted with uranyl acetate and lead citrate and observed using an FEI Quanta 250 FEG scanning electron microscope (FEI, Eindhoven). The imaging settings were as follows: accelerating voltage, 10kV; spot size, 5; image dimensions, 4096x4096; pixel dwell time, 10μs.

FIB-SEM tomography was done with a Helios 650 (FEI, Eindhoven). Fibbing conditions were 30 keV, 770 pA, 30-40 nm slice thickness (specified in text for each experiment) at a tilt angle of 52° and a working distance of 13 mm. For imaging the block face was tilted normal towards the electron beam (Kizilyaprak et al., 2015). The imaging conditions were: 2 keV, 800 pA, 20 μs dwell time, with a frame size of 6144 x 4096 and a pixel size of 9.7 mm. For publication, the image contrast was inverted.

IMOD (Kremer et al., 1996) was used to convert raw data from sequential sections to an MRC file stack and also used for alignment of serial sections and volumetric rendering. Adobe Photoshop was used for image adjustment, layers superposition, annotations, pseudo-coloring of image zones, and volume reconstructions.

Volumetric rendering of FIB-SEM images

Serial sections were stacked and aligned using the cross-correlation function of IMOD, which was also used to trace and reconstruct specific regions. Drawing tools were used for outlining subcellular features (e.g., septate junctions, plasma membrane, nuclei, PAAC) on the EM layers. The 3D reconstruction surfaces were Meshed in Model View/ Objects tool. Images were captured using the Model View/Movie Montage tool and reformatted into .avi format using Fiji.

FUNDING SOURCES

P.M.R. was supported by a Stanford Bio-X Bowes Graduate Fellowship, an EMBO Short-Term Travelling Fellowhsip, and a Stanford DARE Graduate Fellowship (Diversifying Academia, Recruiting Excellence). The authors acknowledge the financial support by the Faculty of Biology and Medicine of the University of Lausanne and of the Swiss National Science Foundation, R'Equip Grant 316030_128692. This work was supported by NIH R01GM116000-01A1, NIH R35GM141885-01, and ACS RSG-17-167-01 to L.E.O.

ACKNOWLEDGEMENTS

We are grateful to Allison Bardin, David Bilder, Nicolas Buchon, Joaquin de Navascues, Mikio Furuse, Yoshihiro Inoue, Henri Jasper, Sarah Siegrist, Norbert Perrimon, Nicolas Tapon, Charles Xu, and Drosophila stock centers (Bloomington *Drosophila* Stock Center (NIH P40OD018537), Vienna Drosophila Resource Center (Dietzl et al., 2007), Kyoto Drosophila Genomics and Genetic Resoruces)for fly stocks; Mikio Furuse, Claire Thomas, Steven Russell, and Xiaohang Yang for antibodies; and Jon Mulholland and Kitty Lee for microscopy support. Confocal microscopy was performed at the Stanford Beckman Cell Sciences Imaging Facility (NIH 1S10OD01058001A1, NIH 1S10OD010580). We thank David Bryant, Tobias Reiff, Daniel St. Johnston, Jia Chen, and members of the O'Brien lab for invaluable discussions. Fly extract was obtained from the *Drosophila* Genomics Resource Center (NIH 2P40OD010949).

FIGURES and CAPTIONS

Figure 1

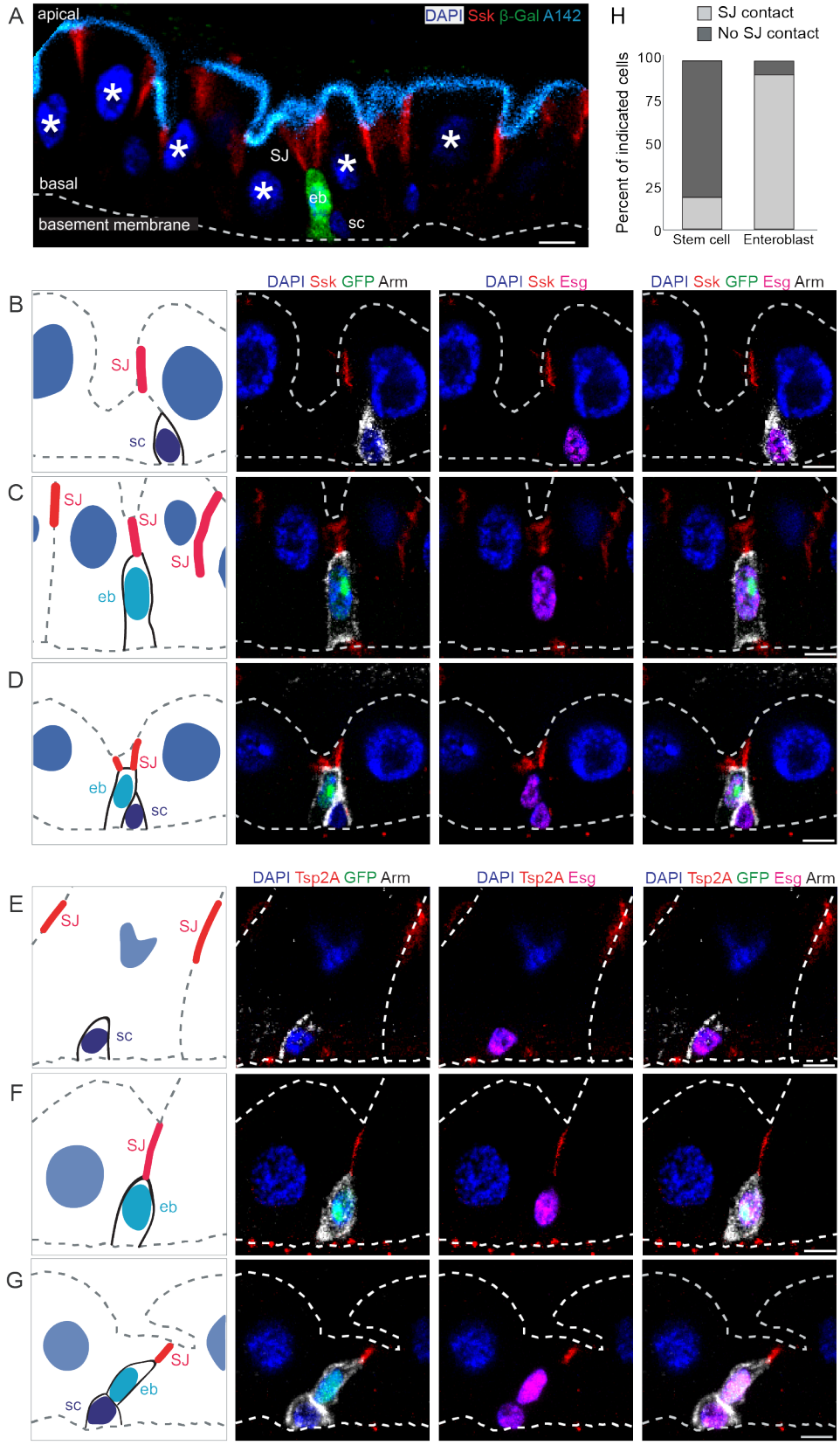

Figure 1. The apical tip of a differentiating enteroblast contacts the SJ of its neighbor enterocytes.

(A) Architecture and stem cell lineage of the fly midgut epithelium, shown in cross-sectional view with apical lumenal surface (cyan, Mdu::GFP; *c.f.* Fig. S2) at top and basal surface (dotted line, basement membrane) at bottom. Three cell types make up the absorptive lineage: (1) Stem cells (sc) are basally localized, diploid cells that do not express *Su(H)-lacZ*. (2) Enteroblasts (eb) are terminally committed stem cell progeny. Enteroblasts are transitioning from stem-like cells to enterocytes and are marked by *Su(H)-lacZ* expression (green, β-Gal). Stem cells and enteroblasts often appear in pairs. (3) Mature enterocytes are large cells with polyploid nuclei (asterisks). Septate junctions (SJ; red, Snakeskin) appear at the apico-lateral borders of enterocytes.

(B-G) Stem cells do not overlap with SJs, while the apical tips of enteroblasts contact the basal termini of enterocyte-enterocyte SJs. Cartoons (left column) and channel overlays from 5-channel multi-photon laser microscopy of *esgGAL4, UAS-his2b::CFP; Su(H)-GFP:nls* midguts immunostained for SJ components Ssk (red, B-D) or Tsp2a (red, E-G) and for the stem cell/enteroblast marker Arm (white; cortical). *esg*-driven His2b::CFP is shown in magenta, *Su(H)*-driven GFP:nls in green and nuclei (DAPI) in blue. Lumenal epithelial surface and basement membrane are indicated by dotted gray lines. Stem cells (sc) are His::CFP$^+$, Arm$^+$, GFP:nls$^-$ cells in Panels B, D, E, G; enteroblasts (eb) are His::CFP$^+$, Arm$^+$,GFP:nls$^+$ cells in Panels C, D, F, G. Panels D and G show stem cell-enteroblast pairs. All scale bars: 5μm. Images are projections of short confocal stacks. Full genotypes in Table 1.

(H) Quantitation of B-G. Most enteroblasts (92%), but few stem cells (19%) contact the epithelial septate junction network. N=5 midguts; n=119 stem cells and 125 enteroblasts.

Figure 2

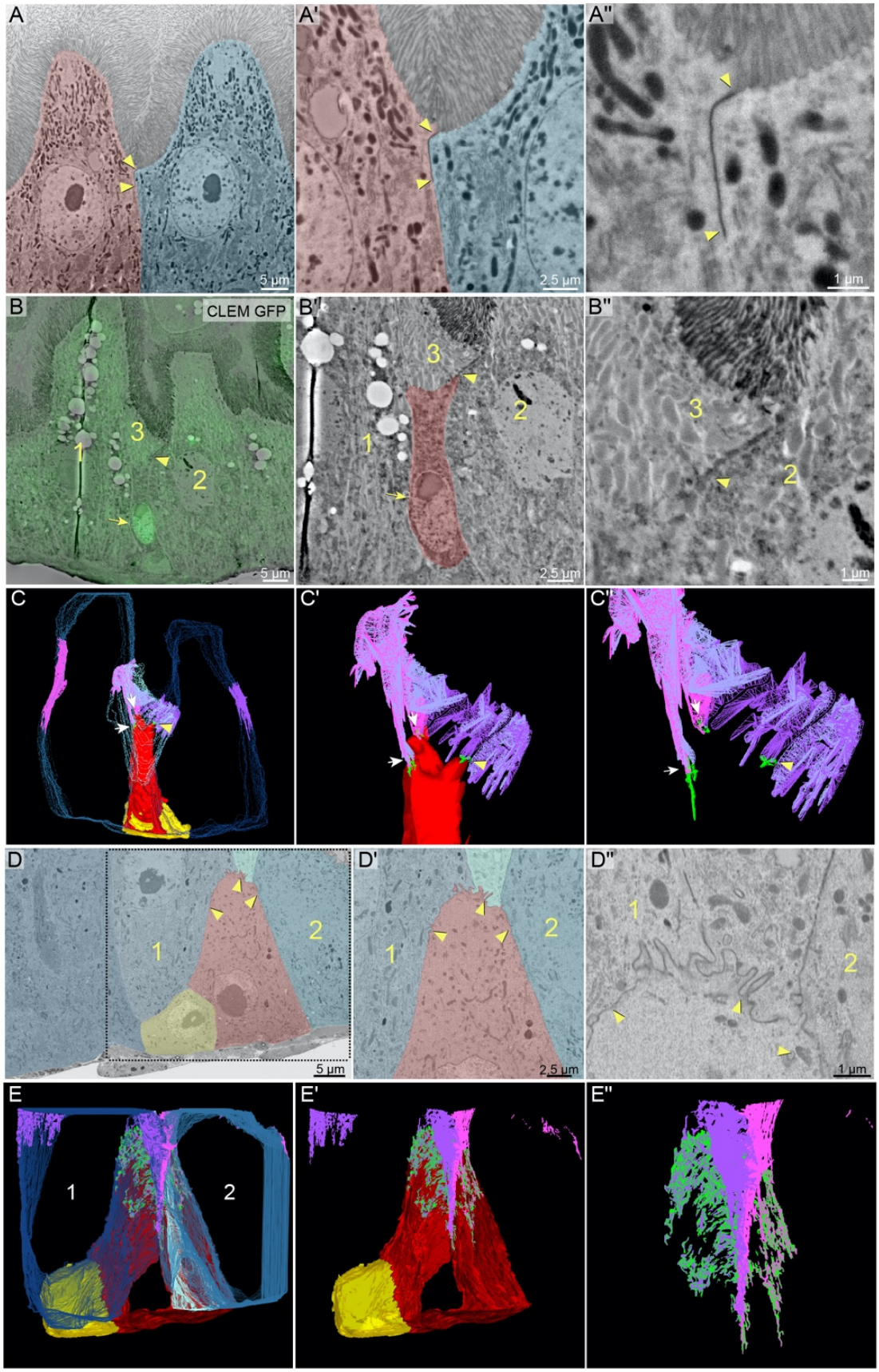
A
A'
A"
5 µm
2.5 µm
1 µm
B
CLEM GFP
B'
B"
1
2
3
5 µm
2.5 µm
1 µm
C
C'
C"
D
D'
D"
1
2
5 µm
2.5 µm
1 µm
E
E'
E"
1
2

Figure 2. The differentiating enteroblast's apex initiates a new SJ at the basal-most edge of mature enterocyte SJs and triggers their remodeling to form a basally-extended SJ sheet.

(A) Mature enterocytes localize SJs to the boundary between lumen-facing, brush border apical membranes and lateral membranes. SEM shows two mature enterocytes (pink and blue pseudocolor). Apical membranes are identifiable as microvilli-rich brush borders. An electron-dense SJ (arrowheads) fuses together the enterocytes' lateral membranes at a site directly adjacent to these brush borders. Zoomed-in views of SJ in A are shown in A′ and A′′.

(B-C) The apex (apical-most tip) of a young, Su(H)$^{+}$ enteroblast initiates SJ adhesions at the basal edge of enterocyte SJs. CLEM overlay (B) identifies a Su(H)-GFP::nls^{+} enteroblast (arrow) in a FIB- SEM section. Zoomed-in images of the enteroblast (B′, red pseudocolor) and of the enteroblast apex (B′′) show a nascent SJ (arrowheads in B-B′′) between the enteroblast and neighbor enterocytes 2 and 3 (labelled). (Only a small wedge of enterocyte 3 is visible in this section.) See Fig. S1. Volumetric rendering (C) of 30 FIB-SEM sections, including the section in B, reveals that each of apex's three fingers forms a SJ (arrows and arrowhead; arrowhead points to the same SJ in B and C) with each of three neighbor enterocytes. Cells and SJs are color coded: enteroblast, red; enteroblast SJs, green; enterocytes 1-3, blue; enterocyte 1 SJs, magenta; enterocyte 2 SJs, light purple; enterocyte 3 SJs, light blue; stem cell, yellow. Zoomed-in views of the enteroblast apex and associated SJs are shown in C′ and C′′. See Video 1.

(D-E) An older enteroblast is blanketed by the broad, basally extended SJ it has formed with the lateral membranes of neighboring mature cells. A FIB-SEM section (D) shows an enteroblast (red pseudocolor), two mature enterocytes (cells 1 and 2; blue pseudocolor), a mature enteroendocrine cell (cell 3; light blue pseudocolor), and a presumptive stem cell (yellow pseudocolor). The apical third of the enteroblast has formed an SJ (arrowheads in D-D′′) with the lateral membranes of the mature cells. Zoomed-in views of the enteroblast apex are shown in D′ and D′′. Volumetric rendering (E) of 413 FIB-SEM sections, including the section in D, reveals basal extensions of both enteroblast-enterocyte SJs and associated enterocyte-enterocyte SJs. View of the SJ with only the enteroblast and stem cell is shown in E′. Zoomed-in view of the SJ alone is shown in E′′. Cells and SJs are color coded: enteroblast, red; enteroblast SJ, green; enterocytes 1 and 2, blue; enterocyte 1 SJ, lavender; enterocyte 2 SJ, magenta; enteroendocrine cell, light blue; stem cell, yellow. See Video 2. Full genotypes in Table 1.

Figure S1 (related to Figure 2C)

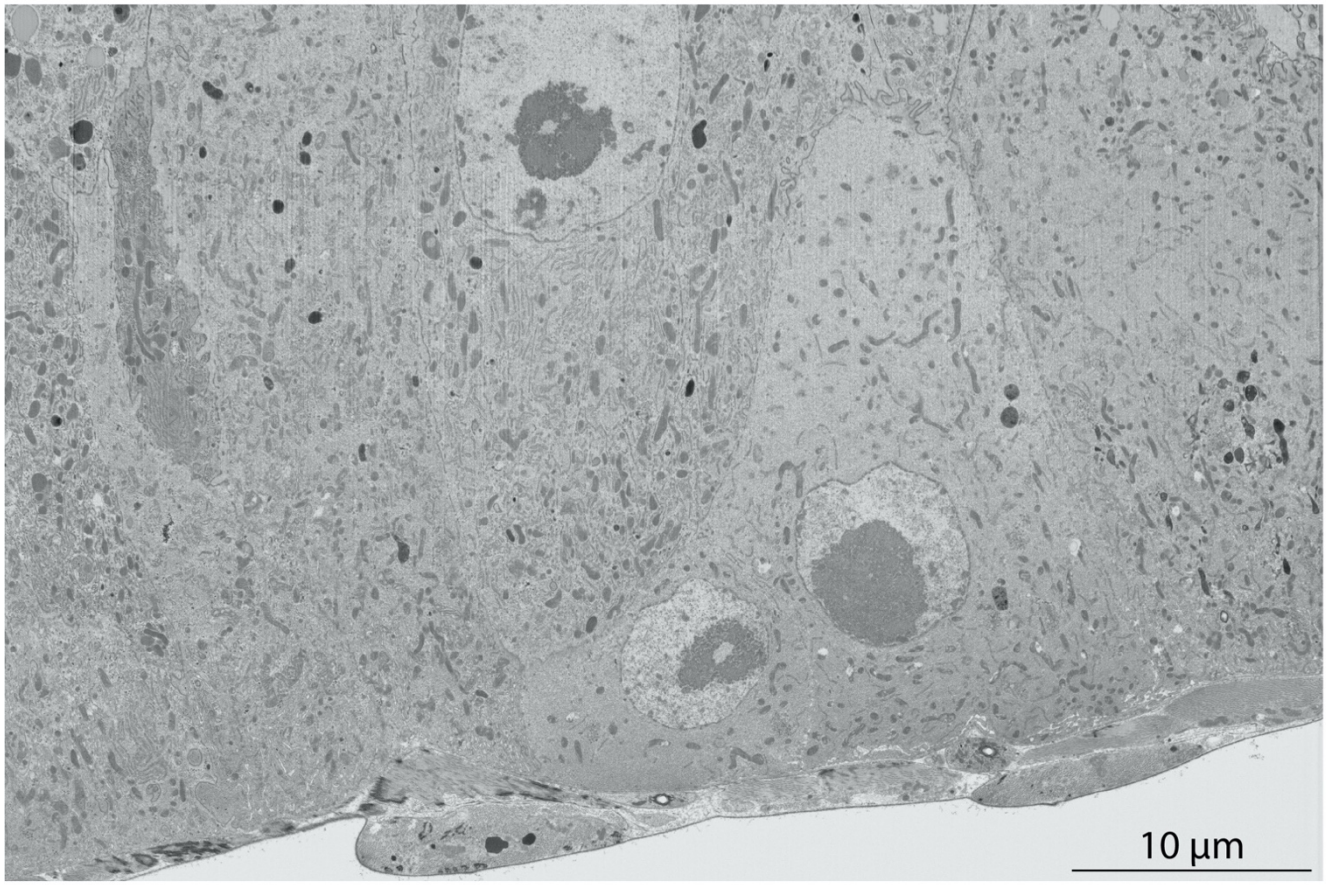

Figure S1 (related to Figure 2D). High resolution view of FIB-SEM section shown in Figure 2D.

30 nm-thick sections were cut with a gallium ion beam at 30 keV and 770 pA. Images were taken with the electron beam at 2 keV, 0.8 nA, 2 mm working distance, 20 μs dwell time, 6144x4096 pixel frame size. Pixel size 9.7nm. Full genotypes in Table 1.

Video 1 (related to Figure 2C). Three-dimensional ultrastructure of nascent SJ between Su(H)-GFP::nls^{+} enteroblast and mature enterocytes.

Tomographic reconstruction of 30 serial images, including the image in Fig. 2B, from midgut expressing *Su(H)-GFP::nls*. Serial sections were cut with a gallium ion beam at 10kV, spot size 5, pixel frame size 4096x4096, pixel dwell time 10μs. Pixel size 8.7nm. Slice thickness, 150nm. Volume of reconstruction, 35.6um x 35.6um x 4.5μm. Full genotypes in Table 1.

Video 2 (related to Figure 2E). Three-dimensional ultrastructure of SJ 'cap' between enteroblast and mature cells.

Tomographic reconstruction of 413 serial FIB-SEM images, including the image shown in Figs. 2C and S1. Volume of reconstruction, 55 μm x 36.6 μm x 12.3 μm. Slice thickness, 30nm. Full genotypes in Table 1.

839 **Figure 3**

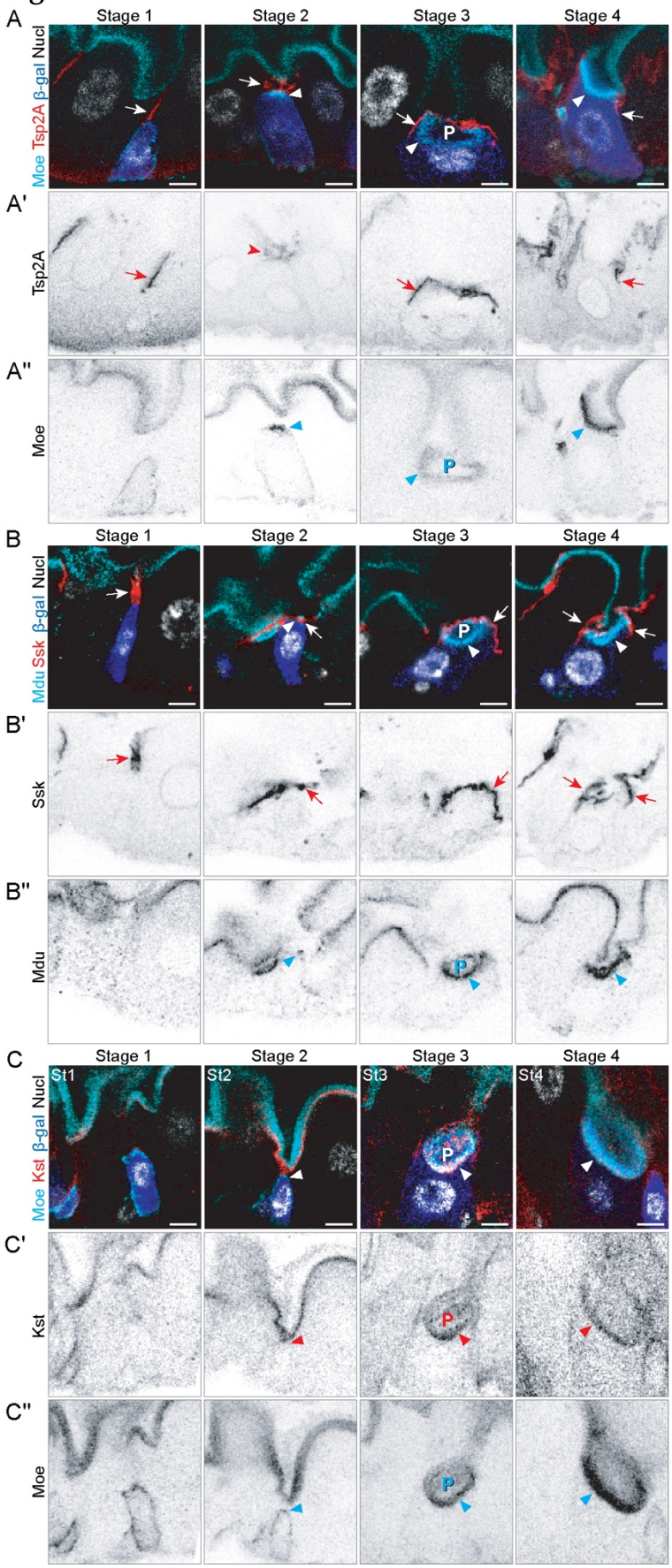

840

841 **Figure 3. SJ and apical membrane morphology define four stages of barrier integration.**

842 As differentiating cells integrate, they pass through four morphological stages that are
843 distinguishable by SJ localization, polarization of apical markers, and cellular/nuclear size. SJs
844 shown in red (A, Tsp2A; B, Ssk). Markers of enterocyte apical polarity shown in either cyan (A, C
845 Moe::GFP; B, Mdu::GFP; *c.f.* Fig. S2) or red (C, Kst). Su(H)-lacZ in blue (β-Gal, A-C). Nuclei (Nucl)
846 shown in grayscale (A, Stage 1 and C – His2av::mRFP; A, Stages 2-4 and B – DAPI). Images are
847 projections of short confocal stacks. Markers that are not fused to a fluorescent protein were
848 visualized by immunostaining. All scale bars, 5 μm. β-gal channel shown in Fig. S3. Full genotypes
849 in Table 1.

850 Stage 1 (St1). Enteroblast with initial SJ contact. The apex of a diploid enteroblast contacts the
851 basal terminus of an enterocyte-enterocyte SJ (arrows). Apical markers are either non-polarized
852 (Moe, Kst) or absent (Mdu).

853 Stage 2 (St2). Enteroblast with broadened SJ contacts and apical plaque. The enteroblast apex
854 is partially covered by a widened enteroblast-enterocyte SJ (arrows). Some apical markers (Moe,
855 Mdu; arrowheads) become polarized to the apex, forming a plaque immediately basal to the SJ.

856 Stage 3 (St3). Pre-enterocyte with umbrella-like SJ and concave apical structure (PAAC). The
857 apex of the cell is fully covered by a convex SJ (arrows). Apical markers outline a prominent concave
858 structure (P; Pre-Assembled Apical Compartment, or PAAC) beneath the SJ. The PAAC fills the
859 apex of the cell and is separate from the gut lumen (Video 3). Pre-enterocytes exhibit
860 cytoplasmic/nuclear sizes intermediate between enteroblasts and mature enterocytes and low
861 *Su(H)*-driven β-gal signal (Fig. S3).

862 Stage 4 (St4). Pre-enterocyte integration becomes complete. The SJ circumscribes the cell, and
863 the PAAC has coalesced with the gut lumen. The pre-enterocyte is still smaller than mature
864 enterocytes and has a concave, rather than convex apical-lumenal surface, but the relative
865 arrangement of its SJ, apical, and basolateral surfaces are topologically equivalent to a mature
866 enterocyte.

867

868 **Figure S2**

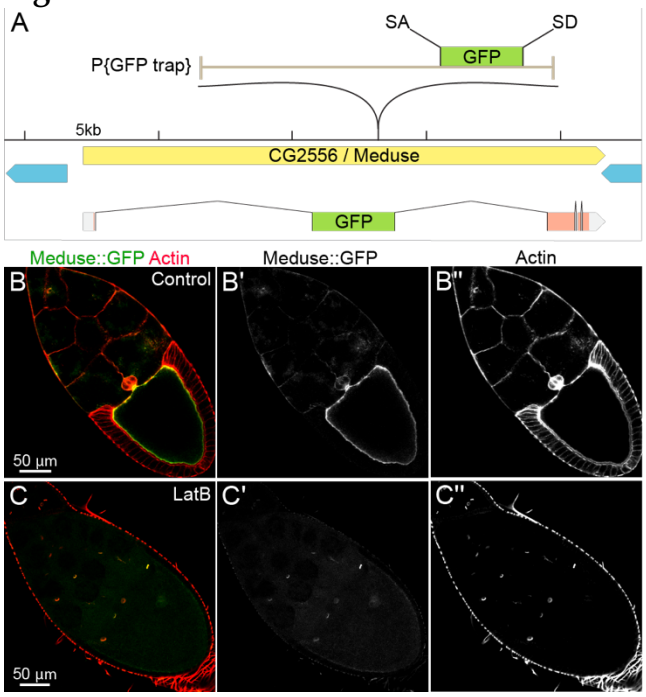

869

870 **Figure S2 (related to Figure 3A-C). The A142 splice trap transposon is inserted into**
871 **CG2556/Meduse, a novel protein that co-localizes with actin filaments.**

872 (A) Genomic location of the splice trap transposon in the A142 line. The insertion was
873 mapped by inverse PCR and genomic PCR to the large first intron of CG2556, approximately 10.6 kb
874 downstream of the splice site in Exon 1. The transposon is inserted in the proper orientation to
875 capture transcripts from CG2556, which would result in an N-terminal GFP tag on the nearly
876 undisrupted protein (Exon 1 encodes only 7 amino acids including the initiator Met). The tentacular
877 appearance of the fusion protein in oocytes prompted us to name the gene Meduse (Mdu).

878 (B) Mdu::GFP co-localizes with cortical actin filaments in Stage 10 oocytes.

879 (C) Latrunculin B (LatB) treatment disrupts cortical actin filaments (red, Rhodamin-
880 phalloidin) in the oocyte and leads to abrogation of the oocyte Mdu::GFP signal. Note that LatB does
881 not disrupt actin in ring canals; localization of Mdu::GFP to ring canals is visible in Panels C and C′.
882 Full genotype in Table 1.

883

884 **Figure S3 (related to Figure 3A-C)**

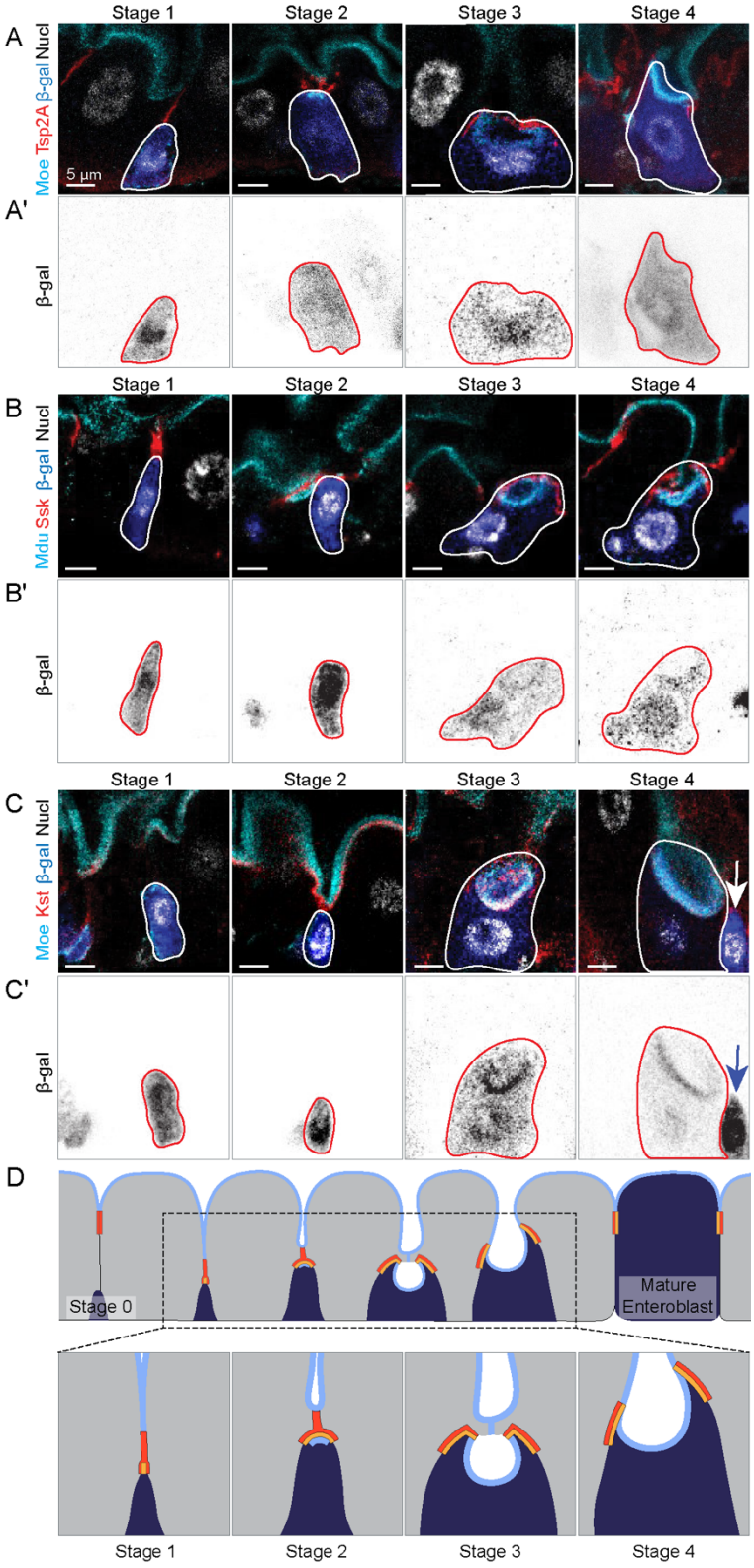

885

886 **Figure S3 (related to Figure 3A-C). Immunostaining of *Su(H)*-driven β-galactosidase in**
887 **integrating cells.**

888 (A-C) The same four-channel images shown in Figure 3 are repeated above the
889 corresponding, single-channel images of β-galactosidase immunostain. The presence of

890 β-galactosidase in Stage 3 and Stage 4 cells demonstrates that these cells derived recently from
891 enteroblasts. During acquisition of the Stage 3 and 4 images, the gain was increased compared to
892 Stages 1 and 2 to visualize lower levels of β-galactosidase. Arrowheads in C and C′ point to a Stage 1
893 enteroblast next to the Stage 4 pre-enterocyte; at the higher gain necessary to visualize β-
894 galactosidase in the Stage 4 pre-enterocyte, β-galactosidase intensity in the Stage 1 enteroblast is
895 overexposed. Images are projections of short confocal stacks.

896 (D) Four-stage model of epithelial integration. A newborn enteroblast (Stage 0) forms SJ
897 contacts between their apex and the basal edge of enterocyte-enterocyte SJs (Stage 1). The
898 enteroblast-enterocyte SJ broadens, and apical markers accumulate at its cytoplasmic face (Stage 2).
899 The enteroblast grows into a pre-enterocyte, characterized by the expansion of apical markers into a
900 PAAC and broadening of the SJ into a diaphragm-like sheet (Stage 3). The PAAC's lumen fuses with
901 the gut's central lumen, and SJs remodel to circumscribe the cell (Stage 4). Eventually, the concave
902 lumenal-apical surface everts to form the convex apical surface that characterizes mature
903 enterocytes. Enteroblast/pre-enterocyte SJs shown in orange, mature enterocyte SJs in red, and
904 apical surface in light blue. Full genotypes in Table 1.

905

906 **Video 3 (related to Figure 3A). 360º confocal reconstruction of a Stage 3 pre-enterocyte**
907 **shows that the PAAC's apical membrane is distinct from the gut's lumenal-apical surface.**

908 Video shows reconstructed 360º view of a Stage 3 pre-enterocyte, labeled by Su(H)-driven
909 β-galactosidase. The pre-enterocyte is surrounded by two mature enterocytes, and a pair of small,
910 basal progenitor cells is visible between the pre-enterocyte and one of the mature enterocytes. The
911 apical marker Moesin::GFP outlines the lumenal-apical surface of the mature enterocytes, the PAAC
912 in the pre-enterocyte, and the entire cortex of the progenitor cells. The SJ protein Tetraspanin2A
913 forms a convex web that covers the apex of the pre-enterocyte. Nuclei are labelled with DAPI. Full
914 genotype in Table 1.

915

Figure 4

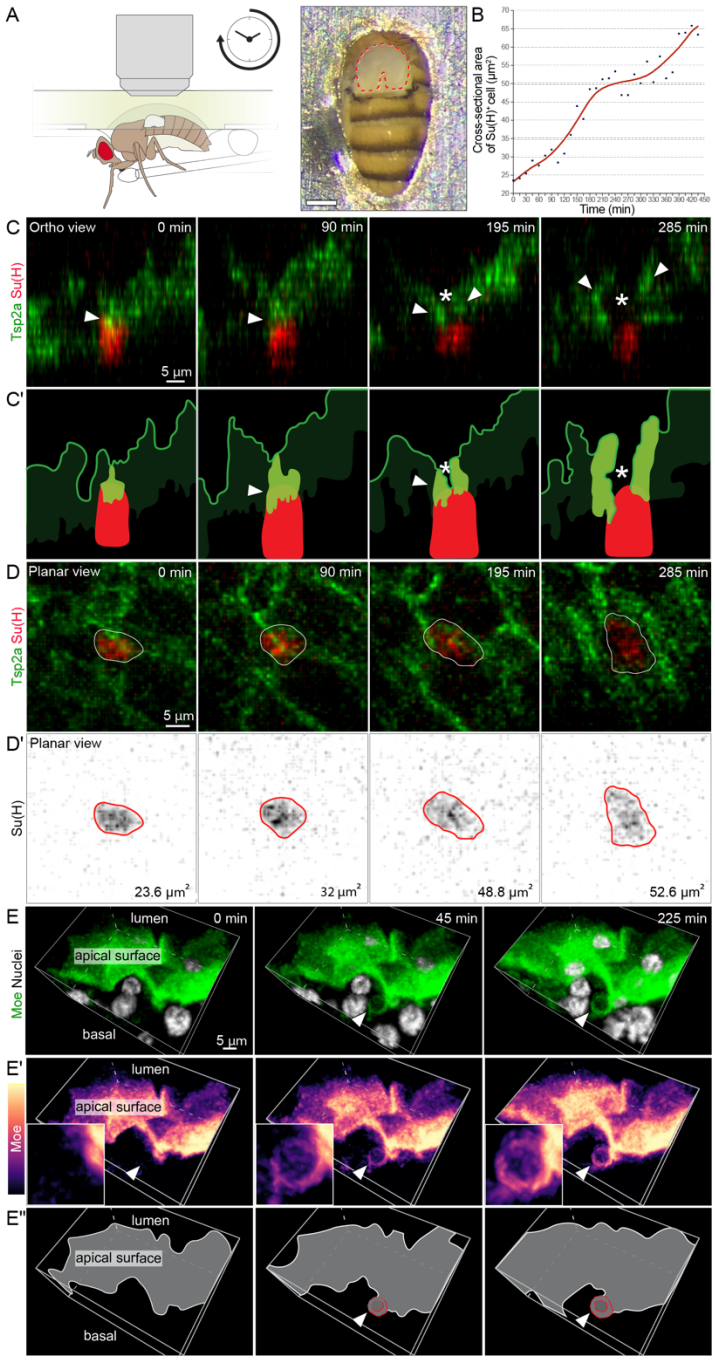

Figure 4: *In vivo* live imaging of SJ and PAAC dynamics supports the four-stage model of integration.

(A) Continuous time-lapse imaging of midguts in live, feeding *Drosophila* was performed through a window in the dorsal cuticle. Adapted from Martin, 2018.

(B) Cross-sectional area of the *Su(H)-mCherry*$^{+}$ cell shown in Panels C and D and in Video 4. The increase in area implies that this cell is actively differentiating from enteroblast to enterocyte.

(C-D) Live dynamics of SJ during enteroblast-enterocyte differentiation. Still frames are from a 7.25 h volumetric movie (Video 4) of a midgut expressing *GS5961-tsp2A::GFP* and *Su(H)-mCherry*. The cell analyzed in Panel B is shown in ortho view (C; apical at top) with corresponding line

927 drawings (C'). In ortho view, arrowheads point to the SJ associated with this cell and asterisk
928 denotes estimated location of putative PAAC. The planar view is shown in (D); panels are
929 projections of serial confocal images. Numbers in the lower right corner of panels in D' are cross-
930 sectional areas of the cell at the given time points. SJ morphogenesis over time is visible in the ortho
931 view: Between 0 min and 90 min, the SJ broadens over the cell's apex. At 195 min, a hollow space
932 (asterisk in C) develops along the SJ's apical-basal axis. Between 195 and 225 min, the hollow space
933 widens; both the hollow space and its surrounding SJ elongate along the lateral edges of the now-
934 larger cell.

935 (E) Live imaging of PAAC development. Still frames from a 3.75 h volumetric movie (Video
936 5) of midgut expressing the apical marker *moe::GFP* (green in E; magma LUT in E') and the nuclear
937 marker *ubi-his2av::RFP* (grayscale in E). Corresponding line drawings are in E''. Arrowhead in E'
938 points to the area of PAAC formation, which is also shown as a close-up in the inset. At 0 min, the
939 lumenal-apical surface appears as a lumpy blanket overlying the gut cell nuclei; no PAAC is visible.
940 By 45 min, a putative PAAC has formed at the basal side of the lumenal-apical surface. By 225 min,
941 the PAAC has become deeper and brighter. Insets in E' show close-up views of the developing
942 PAAC. Full genotypes for all panels in Table.

943

944 **Video 4 (related to Figure 4C and 4D). 7.5-hour continuous time-lapse of SJ dynamics**
945 **during enteroblast-enterocyte differentiation.**

946 Windowmount imaging of midgut expressing *GS5961-tsp2A::GFP* and *Su(H)-mCherry*. Planar
947 (top) and ortho (bottom) views of the same tissue volume are shown. In ortho view, the dotted white
948 line indicates the basal surface of the differentiating cell. Arrowhead points to SJs (Tsp2A::GFP)
949 associated with the differentiating, mCherry^{+} cell analyzed in Fig. 4B. Dynamics of the SJ in ortho
950 view are consistent with the four-stage mechanism inferred from Fig. 3: Nascent contact (Stage 1),
951 broadening and expansion over the cell apex (Stages 2-3), and central hollowing and lateral
952 extension (Stage 4). Full genotype in Table 1.

953

954 **Video 5 (related to Figure 4E). 3.75-hour continuous time-lapse movie of PAAC**
955 **development.**

956 Windowmount imaging of midgut expressing *moesin::GFP* and *ubi-his2av::RFP*. The
957 Moesin::GFP channel (magma LUT) is shown without (left) and with (right) the His2av::RFP channel
958 (grayscale). At 30 min, a faint Moesin::GFP-labelled structure (arrowhead) forms at the basal side of
959 the gut's lumenal-apical surface. The concave shape of this structure is similar to PAACs in fixed
960 samples (Fig. 3, Stage 3; Video 3). From 30-225 min, the putative PAAC deepens, and its GFP-
961 labelled boundary brightens and thickens. Full genotype in Table 1.

962

963

964 **Figure 5**

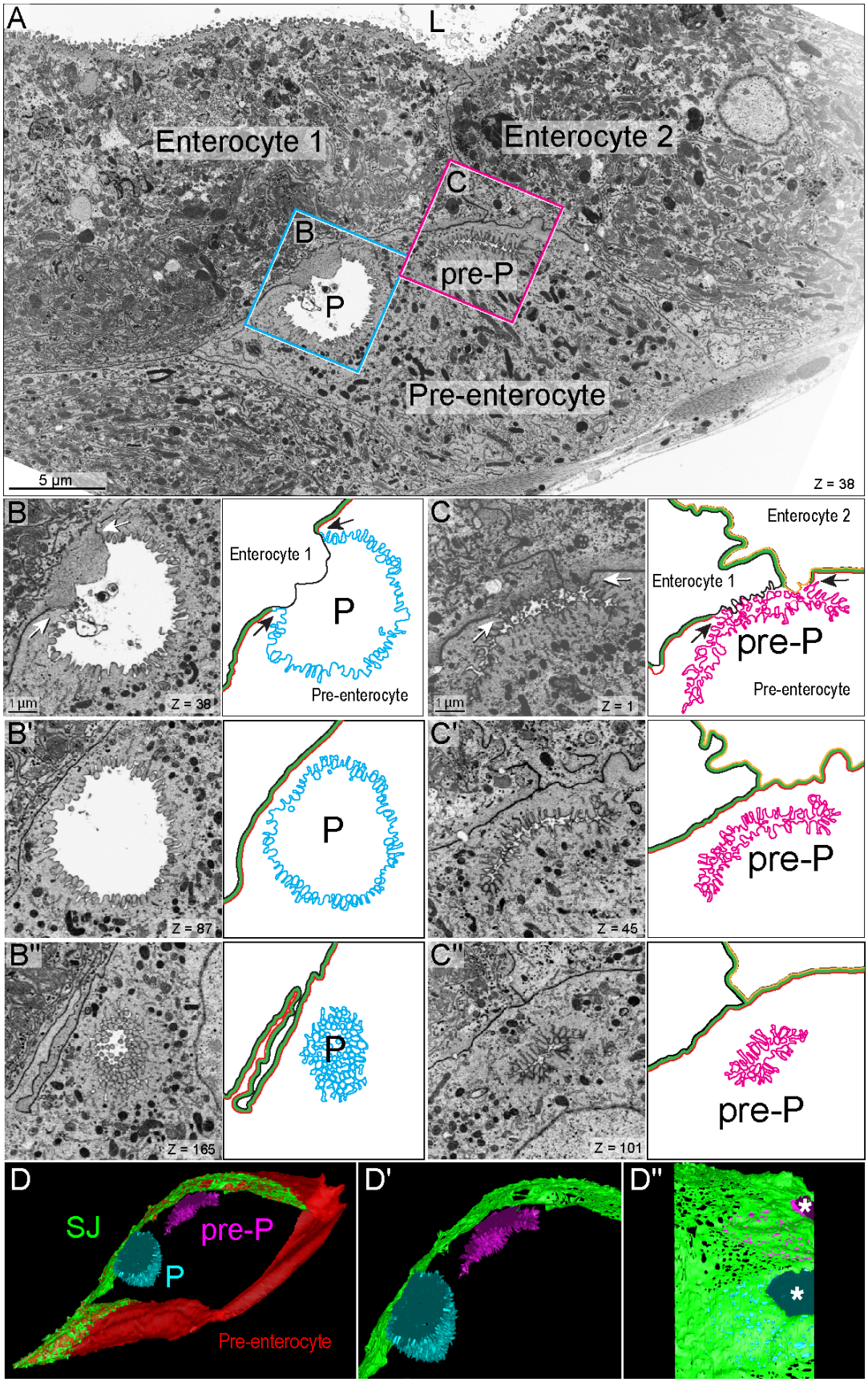

965

Figure 5. PAACs are intercellular lumens with split apical-basolateral polarity.

(A) One slice of a representative, 200-slice FIB-SEM tomographic series. Series captures two mature enterocytes that contact the gut's central lumen (L) and an underlying pre-enterocyte, which does not. An ellipsoid-shaped PAAC (P, cyan box) and an allantoid-shaped PAAC precursor (pre-P, magenta box) appear at the apex of the pre-enterocyte. See Figure S4.

(B) Close-up of the PAAC in cyan box in A. Three FIB-SEM sections are shown next to cartoon representations. P indicates the PAAC lumen. In cartoons, the apical membrane of the pre-enterocyte is cyan, the basolateral membrane of the pre-enterocyte is red, the basolateral plasma membrane of enterocyte 1 is black, and the SJ between the pre-enterocyte and enterocyte 1 is green. In B, a gap in the SJ reveals that the PAAC is an intercellular lumen between the apical pre-enterocyte membrane and the basolateral enterocyte membrane (split polarity). Arrows point to the three-way boundary between the pre-enterocyte apical membrane, the enterocyte basolateral membrane, and the pre-enterocyte basolateral membrane. In B' and B'', the deep cytoplasmic invagination of the pre-enterocyte apical membrane forms most of the PAAC's lumenal volume.

(C) Close-up of the PAAC precursor in magenta box in A. pre-P indicates the PAAC precursor. In cartoons, the pre-enterocyte's apical membrane is magenta, the pre-enterocyte's basolateral membrane is red, the basolateral plasma membrane of enterocyte 1 is black, the basolateral membrane of enterocyte 2 is orange, and the SJ between the pre-enterocyte and enterocytes 1 and 2 is green. In C, a gap in the SJ reveals that the PAAC precursor is an intercellular lumen. Arrows point to two three-way boundaries between the pre-enterocyte apical membrane, the basolateral membrane of either enterocyte 1 or enterocyte 2, and the pre-enterocyte basolateral membrane. In C' and C'', the precursor's slender, allantoid-shaped lumen arises through invagination of the pre-enterocyte's convoluted apical membrane. In A-C, Z values in lower left of panels are slice numbers.

(D) Volumetric rendering of 200 FIB-SEM sections, including the section in A. Apical membranes of the pre-enterocyte are cyan (PAAC) and magenta (PAAC precursor), basolateral membrane of the pre-enterocyte is red, and SJ between the pre-enterocyte and mature enterocytes is in green. Zoomed-in panels show the PAAC, PAAC precursor, and SJ in a cutaway view (D') and a top-down view (D''). In D and D', the PAAC's ellipsoid shape and the precursor's allantoid shape are evident. In D'', asterisks mark holes in the SJ resulting from separation of pre-enterocyte and enterocyte plasma membranes during PAAC formation. (Enterocyte membranes not shown.) See Video 6. Full genotype in Table 1.

Figure S4 (related to Figure 5A)

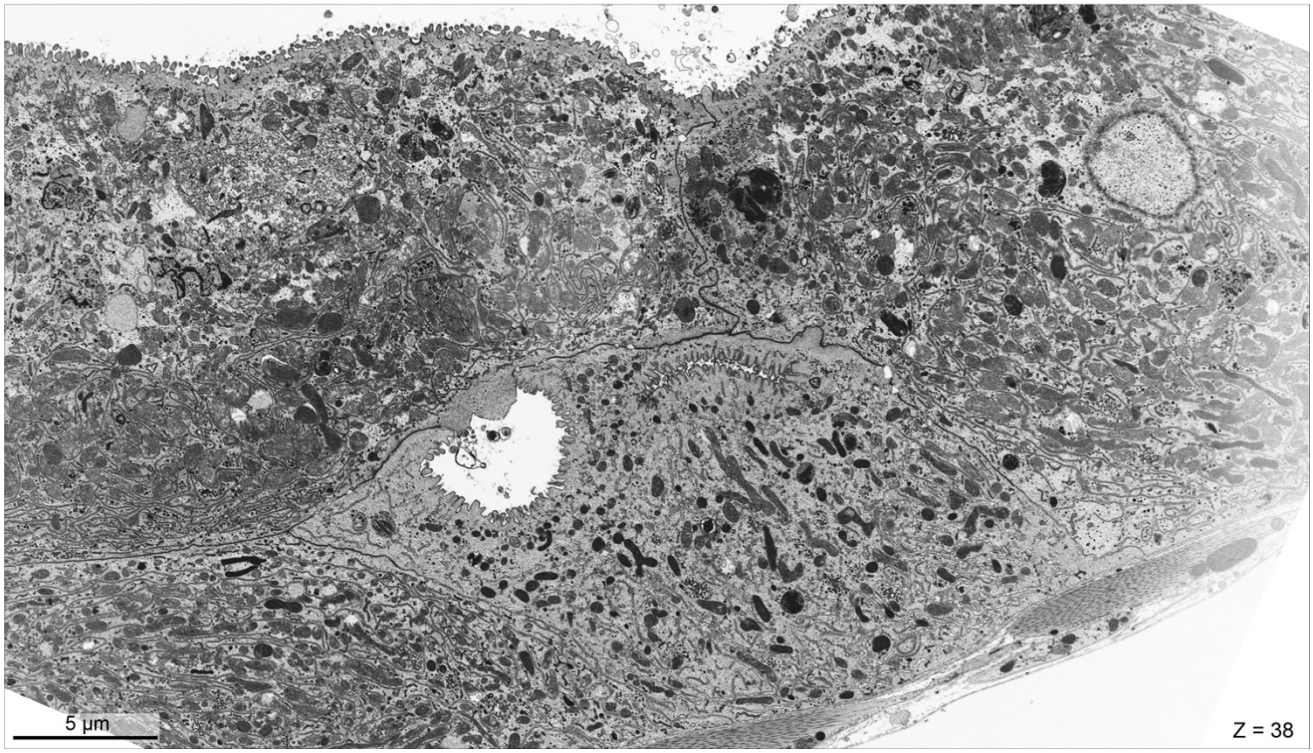

Figure S4 (related to Figure 5A). High resolution view of FIB-SEM section shown in Figure 4A.

40nm-thick sections were cut with a gallium ion beam at 2kV, 0.8 nA, 4.2mm working distance, 5μs dwell time, 6144x4096 frame size. Pixel size 9.7nm. Full genotype in Table 1.

Video 6 (related to Figure 5A-D). Three-dimensional ultrastructure of PAAC, PAAC precursor, and their associated pre-enterocyte.

Tomographic reconstruction of 200 serial FIB-SEM images, including a cropped version of the image shown in Figures 5A and S4. 360º rotation reveals the ellipsoid and allantoid shapes of the PAAC and PAAC precursor, respectively, and also reveals holes in the SJ in which the pre-enterocyte and enterocyte membranes have separated to form the intercellular lumens. Volume of reconstruction: 40.2 μm x 23.9 μm x 8 μm. Slice thickness, 40 nm. Full genotype in Table 1.

Figure 6

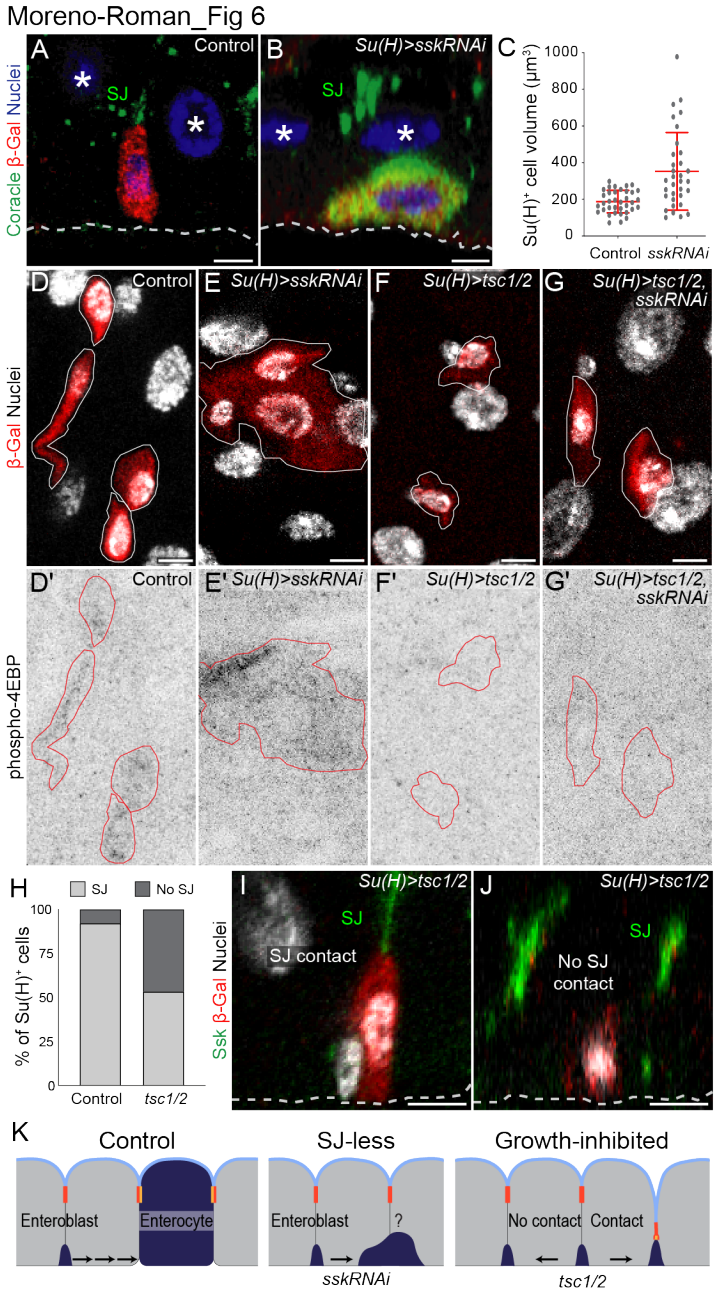

Figure 6. Cells must form SJs and grow in order to integrate.

(A-C) Blocking SJ formation prevents integration but not growth. (A) Cross-sectional view of control *Su(H)*$^{+}$ cell (red, *Su(H)-lacZ*). The cell's apex has formed contacts with the basal tip of the SJ (green, Coracle) between neighbor enterocytes. (B) Cross-sectional view of *Su(H)*^{ts}*>sskRNAi*. The cell expresses *Su(H)-lacZ* (red) and high levels of Coracle (green), which localizes to the cytoplasm. It does not contact either enterocyte-enterocyte SJs or the gut lumen. (C) Measurements of cytoplasmic volumes show that *Su(H)*^{ts}*>sskRNAi* cells become larger in size compared to control *Su(H)* cells.

(D-G) Growth of *Su(H)*^{ts}*>sskRNAi* cells requires Tor pathway activation. Planar views of all midgut cell nuclei (grayscale, DAPI) and *Su(H)-lacZ* (red) are shown above corresponding images of phospho-4EBP immunostain (D'-G', inverted grayscale). *Su(H)-lacZ*-labelled cells are outlined in

white (D-G) and red (D'-G'). Control *Su(H)* cells (D) and *Su(H)^{ts}>sskRNAi* (E) cells are phospho-4EBP^{+} (D', E'). Tor-inhibited, *Su(H)^{ts}>tsc1/2* (F) and *Su(H)^{ts}>sskRNAi, tsc1/2* (G) are not (F', G').

(H-J) Growth-inhibited enteroblasts arrest at initial stages of integration. The frequency with which *Su(H)^{ts}>tsc1/2* cells (*Su(H)-lacZ*, red) contact the gut SJ network (Ssk, green) is reduced to 53% from the control frequency of 92% (H). Both *Su(H)^{ts}>tsc1/2* cells that contact SJs (I) and those that do not (J) fail to reach the gut's lumenal surface. N=3 control midguts (214 enteroblasts) and 3 *Su(H)>tsc1/2* midguts (146 enteroblasts). All scale bars, 5 μm. Full genotypes in Table 1.

(K) Cartoon summary: (Left) Control. Integration requires both cell growth and SJ formation. (Middle) Blocking SJ formation prevents integration but does not halt growth. (Right) Growth inhibition arrests cells in Stages 0-1 of integration.

Figure S5

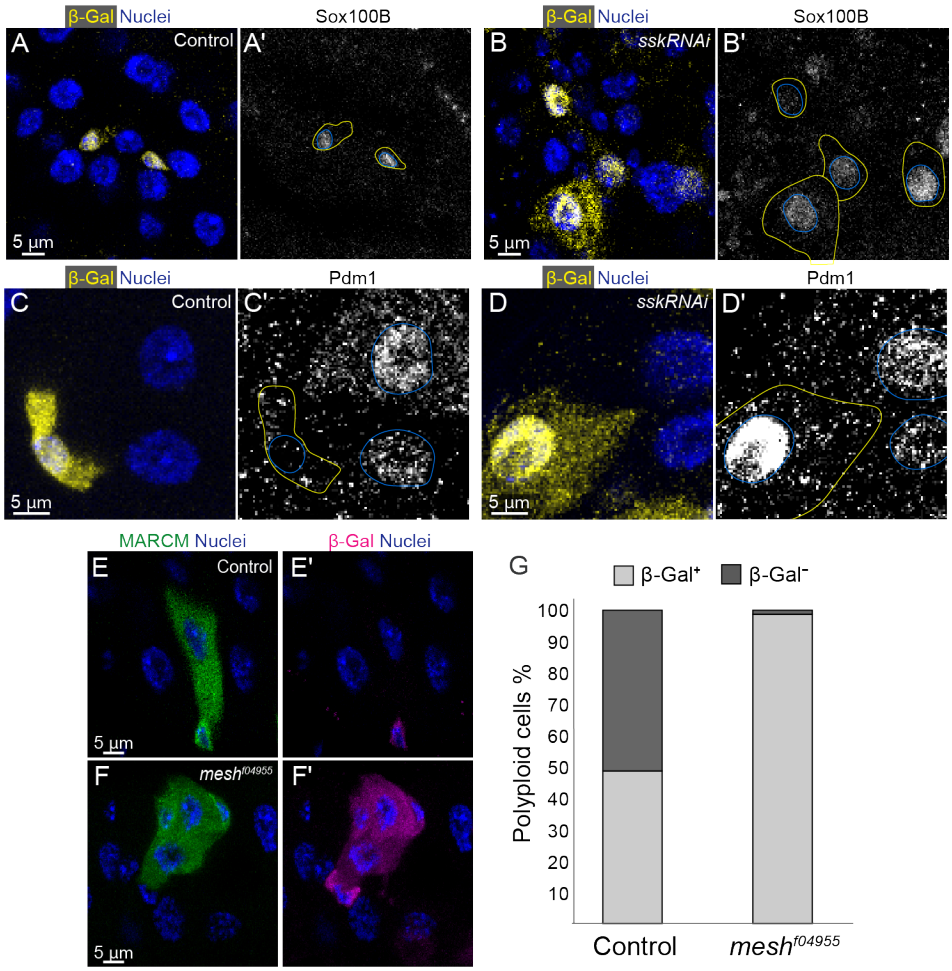

Figure S5 (Related to Figure 6). SJ-less cells exhibit an abnormal mix of enteroblast and enterocyte features.

(A-B) *Su(H)^{ts}>sskRNAi* cells express the stem cell/enteroblast transcription factor Sox100B. Planar views of control *Su(H)* cells (A) and *Su(H)^{ts}>sskRNAi* cells. (B). Left panels: Yellow, *Su(H)-lacZ* (β-gal immunostain); blue, nuclei (DAPI). Right panels: Sox100B immunostain. Yellow and blue outlines in right panels indicate *Su(H)-lacZ*$^{+}$ cells and their nuclei, respectively.

(C-D) *Su(H)^{ts}>sskRNAi* cells express the enterocyte-specific transcription factor Pdm1. Control *Su(H)* cells (C) and *Su(H)^{ts}>sskRNAi* cells are shown. Left panels: Yellow, Su(H)-lacZ (β-gal immunostain); blue, nuclei (DAPI). Right panels: Pdm1 immunostain. Yellow and blue outlines in right panels indicate *Su(H)-lacZ*$^{+}$ cells and their nuclei, respectively.

(E-G) *Su(H)-lacZ* expression in stem cell (MARCM) clones that are either control (E) or *mesh*-null (*mesh^{f04955}*) (E). 4-day clones are labelled with GFP (green). β-gal immunostain (red) identifies *Su(H)-lacZ*-expressing cells. Nuclei are stained with DAPI (blue). In control clones, 52% of polyploid cells have lost β-Gal staining (n=39 polyploid cells from 133 clones, N=3 midguts), implying that terminal differentiation of polyploid cells to enterocyte fate is complete. In *mesh*-null clones, only 1.1% of cells has lost β-gal staining, implying that nearly all cells, despite being polyploid, have not completed terminal differentiation (n=89 polploid cells from 149 clones, N=3 midguts). All scale bars, 5 μm. Full genotypes in Table 1.

Figure 7

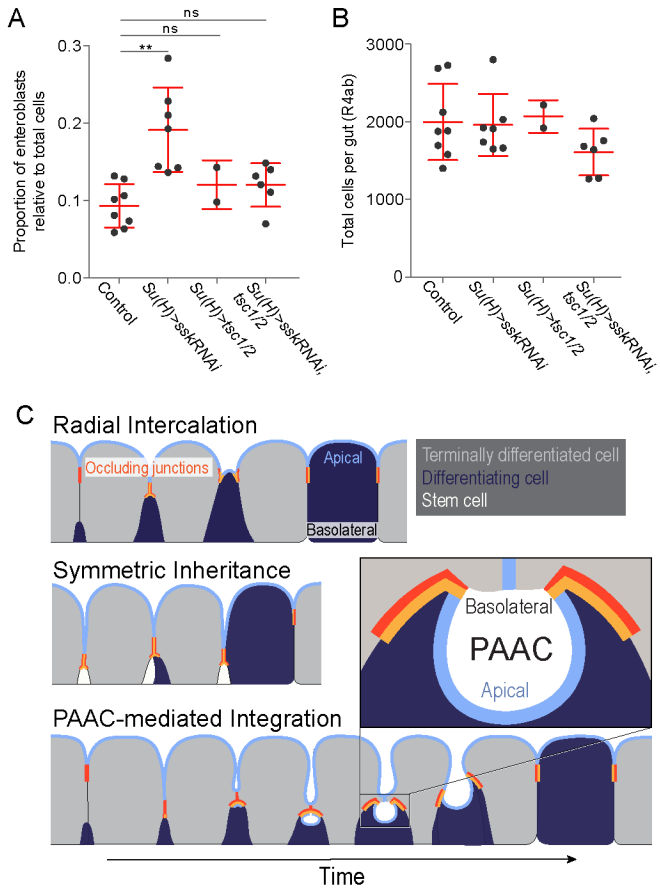

Figure 7. Impact of blocked midgut cell integration on organ-scale cell equilibrium.

(A) Proportion of Su(H)$^{+}$ cells in midguts with blocked cell integration. Plots show the percentage of *Su(H)-lacZ*$^{+}$ cells relative to total cells in the R4ab region of midguts with the indicated genotypes. Cell integration was blocked by inhibiting either new SJ formation (*Su(H)*^{ts}*>sskRNAi*), cell growth (*Su(H)*^{ts}*>tsc1/2*), or both (*Su(H)*^{ts}*>sskRNAi, tsc1/2*) between days 4-8 of adult life. Each data point represents one midgut. Red lines show Means ± S.D for each condition: *Su(H)* control – 0.09 ± 0.03 cells; *Su(H)*^{ts}*>sskRNAi* – 0.19 ± 0.05; *Su(H)*^{ts}*>tsc1/2* – 0.12 ± 0.032 cells; *Su(H)*^{ts}*>sskRNAi, tsc1/2* – 0.12 ± 0.028 cells.

(B) Total numbers of midgut cells remain constant when cell integration is blocked. Plots show total counts of DAPI-labeled nuclei in the R4ab regions of midguts analyzed in Panel A. Each data point represents one midgut. Red lines show Means +/- S.D for each condition: *Su(H)* control – 1997 ± 489 cells; *Su(H)*^{ts}*>sskRNAi* – 1960 ± 398; *Su(H)*^{ts}*>tsc1/2* – 2067 ± 210 cells; *Su(H)*^{ts}*>sskRNAi, tsc1/2* – 1611 ± 299 cells.

(C) Three mechanisms to incorporate stem cell progeny into a mature epithelium. Only PAAC-mediated integration enables the differentiating cell to form new barrier structures (apical plasma membrane and occluding junctions) while still sheltered by the mature occluding junction barrier.

1079 **TABLE 1 – Genotypes in Figure Panels**

FIGURE	GENOTYPE
Fig 1 A	*MduA142GFP/ Su(H)-lacZ* (X Chr)
Fig 1 B-H	*esg-Gal4, UAS-His2b::CFP; Su(H)-GFP::nls*
Fig 2	*esg-Gal4, UAS-His2b::CFP; Su(H)-GFP::nls, ubiP-His2av::mRFP*
Fig 3 A	*Su(H)-lacZ/ +; +; ubiP-His2AV::mRFP, Sqh-Moesin::GFP/ +*
Fig 3 B	*MduA142GFP/ Su(H)-lacZ* (X Chr) *MduA142GFP/ +; Su(H)-Gal4/ +; Su(H)-lacZ, tubP-Gal80ts/ +*
Fig 3 C	*Su(H)-lacZ/ +; +; ubiP-His2AV::mRFP, Sqh-Moesin::GFP/ +*
Fig 4 B-D	*UAS-Tsp2aGFP/ +; Su(H)-mCherry/ 5966GS-Gal4; +*
Fig 4 E	*ubiP-His2Av::mRFP, sqhP-Moe::GFP*
Fig 5	*esg-Gal4, UAS-His2b::CFP; Su(H)-GFP::nls, ubiP-His2av::mRFP*
Fig 6 A	*Su(H)-Gal4, UAS-mCD8::GFP/ +; Su(H)-lacZ, tubP-Gal80ts/ +*
Fig 6 B	*Su(H)-Gal4, UAS-mCD8::GFP/ UAS-sskRNAi; Su(H)-lacZ, tubP-Gal80ts/ +*
Fig 6 C	Same as Fig 6 A&B
Fig 6 D	*Su(H)-Gal4, UAS-mCD8::GFP/ +; Su(H)-lacZ, tubP-Gal80ts/ +*
Fig 6 E	*Su(H)-Gal4, UAS-mCD8::GFP/ UAS-sskRNAi; Su(H)-lacZ, tubP-Gal80ts/ +*
Fig 6 F	*Su(H)-Gal4, UAS-mCD8::GFP/ +; Su(H)-lacZ, tubP-Gal80ts/ UAS-Tsc1/2*
Fig 6 G	*Su(H)-Gal4, UAS-mCD8::GFP/ UAS-sskRNAi; Su(H)-lacZ, tubP-Gal80ts/ UAS-Tsc1/2*
Fig 6 H	**Ctrl:** *esg-Gal4, UAS-His2b::CFP; Su(H)-GFP::nls* ***Su(H)> tsc1/2:*** *Su(H)-Gal4, UAS-mCD8::GFP/ +; Su(H)-lacZ, tubP-Gal80ts/ UAS-Tsc1/2*
Fig 6 I	*Su(H)-Gal4, UAS-mCD8::GFP/ +; Su(H)-lacZ, tubP-Gal80ts/ UAS-Tsc1/2*
Fig 6 J	*Su(H)-Gal4, UAS-mCD8::GFP/ +; Su(H)-lacZ, tubP-Gal80ts/ UAS-Tsc1/2*
Fig 7 A	**Ctrl:** *Su(H)-Gal4, UAS-mCD8::GFP/ +; Su(H)-lacZ, tubP-Gal80ts/ +* ***Su(H)> sskRNAi:*** *Su(H)-Gal4, UAS-mCD8::GFP/ UAS-sskRNAi; Su(H)-lacZ, tubP-Gal80ts/ +* ***Su(H)> tsc1/2:*** *Su(H)-Gal4, UAS-mCD8::GFP/ +; Su(H)-lacZ, tubP-Gal80ts/ UAS-Tsc1/2* ***Su(H)> tsc1/2, sskRNAi:*** *Su(H)-Gal4, UAS-sskRNAi/ +; Su(H)-lacZ, tubP-Gal80ts/ UAS-Tsc1/2*
Fig 7 B	Same as Fig 7 A
Fig 7 C	Same as Fig 7 A
Fig S1	*esg-Gal4, UAS-His2b::CFP; Su(H)-GFP::nls, ubiP-His2av::mRFP*
Fig S2 B&C	*MduA142GFP* (X Chr)
Fig S3	*Su(H)-lacZ/ +; +; ubiP-His2AV::mRFP, Sqh-Moe::GFP/ +*
Fig S4	*esg-Gal4, UAS-His2b::CFP; Su(H)-GFP::nls, ubiP-His2av::mRFP*
Fig S5 A	*Su(H)-Gal4, UAS-mCD8::GFP/ +; Su(H)-lacZ, tubP-Gal80ts/ +*
Fig S5 B	*Su(H)-Gal4, UAS-mCD8::GFP/ UAS-sskRNAi; Su(H)-lacZ, tubP-Gal80ts/ +*
Fig S5 C	*Su(H)-Gal4, UAS-mCD8::GFP/ +; Su(H)-lacZ, tubP-Gal80ts/ +*
Fig S5 D	*Su(H)-Gal4, UAS-mCD8::GFP/ UAS-sskRNAi; Su(H)-lacZ, tubP-Gal80ts/ +*
Fig S5 E	*w, UAS-mCD8::GFP, hsflp^{122}/ Su(H)-lacZ; tubP-Gal4/ +; FRT82B/ FRT82B, tubP-Gal80*
Fig S5 F	*w, UAS-mCD8::GFP, hsflp^{122}/ Su(H)-lacZ; tubP-Gal4/ +; mesh^{f04955}/ FRT82B, tubP-Gal80*
Fig S5 G	Same as Fig S5 E&F

1080

1081

1082 **TABLE 2 – Reagents and Resources**

REAGENT or RESOURCE	SOURCE	IDENTIFIER
Antibodies		
Mouse anti-Armadillo	DSHB	N2 7A1; RRID: AB_528089
Mouse anti-Coracle	DSHB	C615.16; RRID: AB_1161644
Mouse anti-β-galactosidase	Promega	Z3781; RRID: AB 430877
Donkey anti-mouse Alexa Fluor 647	Invitrogen	A-31571; RRID: AB 162542
Donkey anti-rabbit Alexa Fluor 555	Invitrogen	A-31572; RRID: AB_162543
Goat anti-Chicken Alexa Fluor 488	Invitrogen	A-11039; RRID: AB_2534096
Goat anti-Rabbit Alexa Fluor 405	Thermo Fisher	RRID: AB 221605
GFP Polyclonal Antibody, Alexa Fluor 488	Thermo Fisher	A-21311; RRID: AB_221477
Goat anti-Mouse Alexa Fluor 405	Thermo Fisher	A-31553; RRID: AB 221604
Goat anti-Mouse Alexa Fluor 647	Thermo Fisher	A-21240; RRID: AB_2535809
Goat anti-Mouse Alexa Fluor 555	Thermo Fisher	A-21137; RRID: AB_2535776
Goat anti-Rabbit Alexa Fluor 647	Thermo Fisher	A-21244; RRID: AB 2535812
Rabbit anti-Phospho4EBP1	Cell Signaling Technology	RRID: AB 560835
Rabbit anti-Pdm1	Yang lab	N/A
Rabbit anti-Snakeskin	Furuse lab	N/A
Rabbit anti-Tetraspanin2A	Furuse lab	N/A
Rabbit anti-Sox100B	Russell lab	N/A
Rabbit anti-Karst	Thomas lab	N/A
Chemicals, Peptides, and Recombinant Proteins		
Rhodamine Phalloidin	Invitrogen	R415; CAS Number 219920-04-4
RU486	Sigma-Aldrich	M8046-100MG; CAS Number 84371-65-3
DAPI	Thermo Fisher	RRID: AB_2629482
Prolong Gold antifade	Thermo Fisher	P10144
Isradipine	Millipore Sigma	I6658; CAS Number 75695-93-1
Experimental Models: Organisms/Strains		
Drosophila: mesh^{f04955}	BDSC	18826; FLYB: FBti0042412
Drosophila: SqhP-Moesin::GFP	BDSC	59023; FLYB: FBti0016051
Drosophila: Su(H)-Gal4	BDSC	93377; FLYB: FBti0204714
Drosophila: ubiP-His2av::mRFP	BDSC	FLYB: FBti0077846; RRID: BDSC 23650
Drosophila: Su(H)-lacZ (3rd Chr)	BDSC	83352; FLYB: FBtp0014034
Drosophila: tubP-Gal80ts	BDSC	7017; FLYB: FBti0027797
Drosophila: UAS-SskRNAi	VDRC	105193; PMID: 22328496
Drosophila: esg-Gal4	Kyoto DGGR	112304; FLYB: FBti0033872
Drosophila: UAS-His2b::CFP	Yoshihiro Inoue lab	PMID: 24850412
Drosophila: FRT82B	David Bilder lab	FLYB: FBti0002074
Drosophila: UAS-mCD8GFP	David Bilder lab	FLYB: FBtp0002652
Drosophila: 5966GS-Gal4	Henri Jasper lab	FLYB: FBti0150384
Drosophila: UAS-Tsc1/2	Nicolas Tapon lab	PMID: 20573703
Drosophila: Su(H)-mCherry	Allison Bardin lab	N/A
Drosophila: Su(H)-lacZ (X Chr)	Sarah Siegrist lab	N/A
Drosophila: MduA142GFP	Nicolas Buchon lab	N/A
Drosophila: UAS-Tsp2aGFP	Norbert Perrimon lab	N/A
Drosophila: Su(H)-GFP::nls	Joaquin de Navascués lab	PMID: 22522699

(*Continued on next page*)

1083

Continued

REAGENT or RESOURCE	SOURCE	IDENTIFIER
Oligonucleotides		
*traF*_U primer: CGAGAAAGAGAA-TACCATGGGCGATCAA	N/A	N/A
*traF*_L primer: CCTGTGGTGGCACTTGCACATAGTA	N/A	N/A
*GFP*_62U primer: CGACGTAAAC-GGCCACAAGTTCA	N/A	N/A
*GFP*_495L primer: CCTCGATGTT-GTGGCGGATCTTGAA	N/A	N/A
3'Pout_U primer: CATA-TCGCTGTCTCACTCAGACTCAA	N/A	N/A
*Mdu*3'conf_L2 primer: CGCGCCACTATGTGCCGCAAA	N/A	N/A
M*du*3'conf_L1 primer: GCCAAAAGGCATAAAAACAGCTAA	N/A	N/A
*Mdu*5'conf_U1 primer: GTGTCAATGGCCCAGAGACCA	N/A	N/A
*Mdu*5'conf_U2 primer: GAAATGGGTATGAACTG-CAAATCAGTA	N/A	N/A
*Mdu*5'conf_U3 primer: GAACAGGCAACAGATGCCCAGA-TAATACA	N/A	N/A
5'Pout_L1 primer: CTTCGGTAAGCTTCGGCTATCGA	N/A	N/A
5'Pout_L2 primer: CTCAACAAGCAAACGTGCACTGAA	N/A	N/A
Software and Algorithms		
Fiji	https://fiji.sc	RRID:SCR_002285
Bitplane Imaris 8	Bitplane	RRID:SCR_007370
IMOD	https://bio3d.colorado.edu/imod/	RRID:SCR_003297
Graphpad Prism 7	GraphPad Software	RRID:SCR_002798

REFERENCES

Akagi, K., Wilson, K.A., Katewa, S.D., Ortega, M., Simons, J., Hilsabeck, T.A., Kapuria, S., Sharma, A., Jasper, H., and Kapahi, P. (2018). Dietary restriction improves intestinal cellular fitness to enhance gut barrier function and lifespan in D. melanogaster. PLOS Genetics *14*, e1007777.

Alvers, A.L., Ryan, S., Scherz, P.J., Huisken, J., and Bagnat, M. (2014). Single continuous lumen formation in the zebrafish gut is mediated by smoothened-dependent tissue remodeling. Development *141*, 1110–1119.

Amcheslavsky, A., Ito, N., Jiang, J., and Ip, Y.T. (2011). Tuberous sclerosis complex and Myc coordinate the growth and division of Drosophila intestinal stem cells. The Journal of Cell Biology *193*, 695–710.

Arganda-Carreras, I., Sorzano, C.O.S., Marabini, R., Carazo, J.M., Ortiz-de-Solorzano, C., and Kybic, J. (2006). Consistent and elastic registration of histological sections using vector-spline regularization. In Computer Vision Approaches to Medical Image Analysis, (Berlin, Heidelberg: Springer, Berlin, Heidelberg), pp. 85–95.

Bachmair, A., Finley, D., and Varshavsky, A. (1986). In vivo half-life of a protein is a function of its amino-terminal residue. Science *234*, 179–186.

Bagnat, M., Cheung, I.D., Mostov, K.E., and Stainier, D.Y.R. (2007). Genetic control of single lumen formation in the zebrafish gut. Nature Cell Biology *9*, 954–960.

Bardin, A.J., Perdigoto, C.N., Southall, T.D., Brand, A.H., and Schweisguth, F. (2010). Transcriptional control of stem cell maintenance in the Drosophila intestine. Development *137*, 705–714.

Baumann, O. (2001). Posterior midgut epithelial cells differ in their organization of the membrane skeleton from other drosophila epithelia. Exp Cell Res *270*, 176–187.

Blasky, A.J., Mangan, A., and Prekeris, R. (2015). Polarized Protein Transport and Lumen Formation During Epithelial Tissue Morphogenesis. Annu. Rev. Cell Dev. Biol. *31*, 575–591.

Bobinnec, Y., Marcaillou, C., Morin, X., and Debec, A. (2003). Dynamics of the endoplasmic reticulum during early development of Drosophila melanogaster. Cell Motility *54*, 217–225.

Bonfini, A., Dobson, A.J., Duneau, D., Revah, J., Liu, X., Houtz, P., and Buchon, N. (2021). Multiscale analysis reveals that diet-dependent midgut plasticity emerges from alterations in both stem cell niche coupling and enterocyte size. ELife *10*, e64125.

Bryant, D.M., Datta, A., Rodríguez-Fraticelli, A.E., Peränen, J., Martín-Belmonte, F., and Mostov, K.E. (2010). A molecular network for de novo generation of the apical surface and lumen. Nat Cell Biol *12*, 1035–1045.

Buchon, N., Osman, D., David, F.P.A., Yu Fang, H., Boquete, J.-P., Deplancke, B., and Lemaitre, B. (2013). Morphological and molecular characterization of adult midgut compartmentalization in Drosophila. Cell Rep *3*, 1725–1738.

Burel, A., Lavault, M.-T., Chevalier, C., Gnaegi, H., Prigent, S., Mucciolo, A., Dutertre, S., Humbel, B.M., Guillaudeux, T., and Kolotuev, I. (2018). A targeted 3D EM and correlative microscopy method using SEM array tomography. Development *145*.

Campbell, K., Casanova, J., and Skaer, H. (2010). Mesenchymal-to-epithelial transition of intercalating cells in Drosophila renal tubules depends on polarity cues from epithelial neighbours. Mech Dev *127*, 345–357.

Chan, C.J., Costanzo, M., Ruiz-Herrero, T., Mönke, G., Petrie, R.J., Bergert, M., Diz-Muñoz, A., Mahadevan, L., and Hiiragi, T. (2019). Hydraulic control of mammalian embryo size and cell fate. Nature *571*, 112–116.

Chen, J., Sayadian, A.-C., Lowe, N., Lovegrove, H.E., and St Johnston, D. (2018). An alternative mode of epithelial polarity in the Drosophila midgut. PLoS Biology *16*, e3000041.

Chepko, G., and Dickson, R.B. (2003). Ultrastructure of the putative stem cell niche in rat mammary epithelium. Tissue and Cell *35*, 83–93.

Chepko, G., and Smith, G.H. (1997). Three division-competent, structurally-distinct cell populations contribute to murine mammary epithelial renewal. Tissue and Cell *29*, 239–253.

Choi, N.-H., Lucchetta, E., and Ohlstein, B. (2011). Nonautonomous regulation of Drosophila midgut stem cell proliferation by the insulin-signaling pathway. Proceedings of the National Academy of Sciences *108*, 18702–18707.

Cotsarelis, G., Cheng, S.-Z., Dong, G., Sun, T.-T., and Lavker, R.M. (1989). Existence of slow-cycling limbal epithelial basal cells that can be preferentially stimulated to proliferate: Implications on epithelial stem cells. Cell *57*, 201–209.

Daniel, E., Daudé, M., Kolotuev, I., Charish, K., Auld, V., and Le Borgne, R. (2018). Coordination of Septate Junctions Assembly and Completion of Cytokinesis in Proliferative Epithelial Tissues. Curr. Biol. *28*, 1380-1391.e4.

Dantoft, W., Davis, M.M., Lindvall, J.M., Tang, X., Uvell, H., Junell, A., Beskow, A., and Engström, Y. (2013). The Oct1 homolog Nubbin is a repressor of NF-κB-dependent immune gene expression that increases the tolerance to gut microbiota. BMC Biology *11*, 99.

Dasgupta, S., Gupta, K., Zhang, Y., Viasnoff, V., and Prost, J. (2018). Physics of lumen growth. PNAS *115*, E4751–E4757.

Datta, A., Bryant, D.M., and Mostov, K.E. (2011). Molecular Regulation of Lumen Morphogenesis. Current Biology *21*, R126–R136.

Deblandre, G.A., Wettstein, D.A., Koyano-Nakagawa, N., and Kintner, C. (1999). A two-step mechanism generates the spacing pattern of the ciliated cells in the skin of Xenopus embryos. Development *126*, 4715–4728.

DeMaio, L., Tseng, W., Balverde, Z., Alvarez, J.R., Kim, K.-J., Kelley, D.G., Senior, R.M., Crandall, E.D., and Borok, Z. (2009). Characterization of mouse alveolar epithelial cell monolayers. American Journal of Physiology-Lung Cellular and Molecular Physiology *296*, L1051–L1058.

Dietzl, G., Chen, D., Schnorrer, F., Su, K.-C., Barinova, Y., Fellner, M., Gasser, B., Kinsey, K., Oppel, S., Scheiblauer, S., et al. (2007). A genome-wide transgenic RNAi library for conditional gene inactivation in Drosophila. Nature *448*, 151–156.

Doupé, D.P., Marshall, O.J., Dayton, H., Brand, A.H., and Perrimon, N. (2018). Drosophila intestinal stem and progenitor cells are major sources and regulators of homeostatic niche signals. PNAS *115*, 12218–12223.

Dumortier, J.G., Verge-Serandour, M.L., Tortorelli, A.F., Mielke, A., Plater, L. de, Turlier, H., and Maître, J.-L. (2019). Hydraulic fracturing and active coarsening position the lumen of the mouse blastocyst. Science *365*, 465–468.

Edwards, K.A., Demsky, M., Montague, R.A., Weymouth, N., and Kiehart, D.P. (1997). GFP-Moesin Illuminates Actin Cytoskeleton Dynamics in Living Tissue and Demonstrates Cell Shape Changes during Morphogenesis inDrosophila. Developmental Biology *191*, 103–117.

Evans, M.J., and Moller, P.C. (1991). Biology of Airway Basal Cells. Experimental Lung Research *17*, 513–531.

Fleming, E.S., Zajac, M., Moschenross, D.M., Montrose, D.C., Rosenberg, D.W., Cowan, A.E., and Tirnauer, J.S. (2007). Planar spindle orientation and asymmetric cytokinesis in the mouse small intestine. J. Histochem. Cytochem. *55*, 1173–1180.

Furuse, M., and Izumi, Y. (2017). Molecular dissection of smooth septate junctions: understanding their roles in arthropod physiology. Ann N Y Acad Sci *1397*, 17–24.

Gilbert, T., and Rodriguez-Boulan, E. (1991). Induction of vacuolar apical compartments in the Caco-2 intestinal epithelial cell line. Journal of Cell Science *100*, 451–458.

Guillot, C., and Lecuit, T. (2013). Mechanics of epithelial tissue homeostasis and morphogenesis. Science *340*, 1185–1189.

He, L., Binari, R., Huang, J., Falo-Sanjuan, J., and Perrimon, N. (2019). In vivo study of gene expression with an enhanced dual-color fluorescent transcriptional timer. ELife *8*, e46181.

Izumi, Y., Motoishi, M., Furuse, K., and Furuse, M. (2016). A tetraspanin regulates septate junction formation in Drosophila midgut. J Cell Sci *129*, 1155–1164.

Jiang, H., and Edgar, B.A. (2009). EGFR signaling regulates the proliferation of Drosophila adult midgut progenitors. Development *136*, 483–493.

Jin, Y., Patel, P.H., Kohlmaier, A., Pavlovic, B., Zhang, C., and Edgar, B.A. (2017). Intestinal stem cell pool regulation in Drosophila. Stem Cell Reports *8*, 1479–1487.

Jin, Z., Chen, J., Huang, H., Wang, J., Lv, J., Yu, M., Guo, X., Zhang, Y., Cai, T., and Xi, R. (2020). The Drosophila Ortholog of Mammalian Transcription Factor Sox9 Regulates Intestinal Homeostasis and Regeneration at an Appropriate Level. Cell Reports *31*.

Jinguji, Y., and Ishikawa, H. (1992). Electron Microscopic Observations on the Maintenance of the Tight Junction during Cell Division in the Epithelium of the Mouse Small Intestine. Cell Struct Funct *17*, 27–37.

Kapuria, S., Karpac, J., Biteau, B., Hwangbo, D., and Jasper, H. (2012). Notch-Mediated Suppression of TSC2 Expression Regulates Cell Differentiation in the Drosophila Intestinal Stem Cell Lineage. PLoS Genetics *8*, e1003045.

Kizilyaprak, C., Longo, G., Daraspe, J., and Humbel, B.M. (2015). Investigation of resins suitable for the preparation of biological sample for 3-D electron microscopy. Journal of Structural Biology *189*, 135–146.

Kolotuev, I. (2014). Positional Correlative Anatomy of Invertebrate Model Organisms Increases Efficiency of TEM Data Production. Microscopy and Microanalysis *20*, 1392–1403.

Kolotuev, I., and Micheva, K.D. (2019). Can Correlative Microscopy Ever Be Easy? An Array Tomography Viewpoint. In Correlative Imaging, (John Wiley & Sons, Ltd), pp. 81–98.

Kolotuev, I., Schwab, Y., and Labouesse, M. (2010). A precise and rapid mapping protocol for correlative light and electron microscopy of small invertebrate organisms. Biology of the Cell *102*, 121–132.

Korzelius, J., Naumann, S.K., Loza-Coll, M.A., Chan, J.S., Dutta, D., Oberheim, J., Gläßer, C., Southall, T.D., Brand, A.H., Jones, D.L., et al. (2014). Escargot maintains stemness and suppresses differentiation in Drosophila intestinal stem cells. EMBO J *33*, 2967–2982.

Koyama, L.A.J., Aranda-Díaz, A., Su, Y.-H., Balachandra, S., Martin, J.L., Ludington, W.B., Huang, K.C., and O'Brien, L.E. (2020). Bellymount enables longitudinal, intravital imaging of abdominal organs and the gut microbiota in adult Drosophila. PLOS Biology *18*, e3000567.

Kremer, J.R., Mastronarde, D.N., and McIntosh, J.R. (1996). Computer Visualization of Three-Dimensional Image Data Using IMOD. Journal of Structural Biology *116*, 71–76.

Lattner, J., Leng, W., Knust, E., Brankatschk, M., and Flores-Benitez, D. (2019). Crumbs organizes the transport machinery by regulating apical levels of PI(4,5)P2 in Drosophila. ELife *8*, e50900.

Leblond, C.P. (1981). The life history of cells in renewing systems. Am. J. Anat. *160*, 114–158.

Lee, T., and Luo, L. (1999). Mosaic analysis with a repressible cell marker for studies of gene function in neuronal morphogenesis. Neuron *22*, 451–461.

Lee, W.-C., Beebe, K., Sudmeier, L., and Micchelli, C.A. (2009). Adenomatous polyposis coli regulates Drosophila intestinal stem cell proliferation. Development *136*, 2255–2264.

Lemaitre, B., and Miguel-Aliaga, I. (2013). The Digestive Tract of Drosophila melanogaster. Annu Rev Genet *47*, 377–404.

Leung, C.T., Coulombe, P.A., and Reed, R.R. (2007). Contribution of olfactory neural stem cells to tissue maintenance and regeneration. Nat Neurosci *10*, 720–726.

Liang, J., Balachandra, S., Ngo, S., and O'Brien, L.E. (2017). Feedback regulation of steady-state epithelial turnover and organ size. Nature *548*, 588–591.

Linden, S.K., Sutton, P., Karlsson, N.G., Korolik, V., and McGuckin, M.A. (2008). Mucins in the mucosal barrier to infection. Mucosal Immunology *1*, 183–197.

Lowery, L.A., Rienzo, G.D., Gutzman, J.H., and Sive, H. (2009). Characterization and Classification of Zebrafish Brain Morphology Mutants. The Anatomical Record *292*, 94–106.

Macara, I.G., Guyer, R., Richardson, G., Huo, Y., and Ahmed, S.M. (2014). Epithelial Homeostasis. Current Biology *24*, R815–R825.

Madara, J.L. (1987). Intestinal absorptive cell tight junctions are linked to cytoskeleton. American Journal of Physiology-Cell Physiology *253*, C171–C175.

Marianes, A., and Spradling, A.C. (2013). Physiological and stem cell compartmentalization within the Drosophila midgut. ELife *2*, 155.

Martin, J.L., Sanders, E.N., Moreno-Roman, P., Jaramillo Koyama, L.A., Balachandra, S., Du, X., and O'Brien, L.E. (2018). Long-term live imaging of the Drosophila adult midgut reveals real-time dynamics of division, differentiation and loss. ELife *7*, e36248.

McGuckin, M.A., Lindén, S.K., Sutton, P., and Florin, T.H. (2011). Mucin dynamics and enteric pathogens. Nature Reviews Microbiology *9*, 265–278.

McGuire, S.E., Le, P.T., Osborn, A.J., Matsumoto, K., and Davis, R.L. (2003). Spatiotemporal rescue of memory dysfunction in Drosophila. Science *302*, 1765–1768.

McKinley, K.L., Stuurman, N., Royer, L.A., Schartner, C., Castillo-Azofeifa, D., Delling, M., Klein, O.D., and Vale, R.D. (2018). Cellular aspect ratio and cell division mechanics underlie the patterning of cell progeny in diverse mammalian epithelia. ELife *7*, e36739.

McMahon, A., Supatto, W., Fraser, S.E., and Stathopoulos, A. (2008). Dynamic Analyses of Drosophila Gastrulation Provide Insights into Collective Cell Migration. Science *322*, 1546–1550.

Meng, F.W., Rojas Villa, S.E., and Biteau, B. (2020). Sox100B Regulates Progenitor-Specific Gene Expression and Cell Differentiation in the Adult Drosophila Intestine. Stem Cell Reports *14*, 226–240.

Merzdorf, C.S., Chen, Y.-H., and Goodenough, D.A. (1998). Formation of Functional Tight Junctions in Xenopus Embryos. Developmental Biology *195*, 187–203.

Micchelli, C.A., and Perrimon, N. (2006). Evidence that stem cells reside in the adult Drosophila midgut epithelium. Nature *439*, 475–479.

Michael J. Evans, C.G.P., Laura S. Van Winkle, Michelle V. Fanucchi (2001). Cellular and Molecular Characteristics of Basal Cells in Airway Epithelium. Experimental Lung Research *27*, 401–415.

de Navascués, J., Perdigoto, C.N., Bian, Y., Schneider, M.H., Bardin, A.J., Martínez-Arias, A., and Simons, B.D. (2012). Drosophila midgut homeostasis involves neutral competition between symmetrically dividing intestinal stem cells. EMBO J *31*, 2473–2485.

Nie, Y., Li, Q., Amcheslavsky, A., Duhart, J.C., Veraksa, A., Stocker, H., Raftery, L.A., and Ip, Y.T. (2015). Bunched and Madm Function Downstream of Tuberous Sclerosis Complex to Regulate the Growth of Intestinal Stem Cells in Drosophila. Stem Cell Rev and Rep *11*, 813–825.

O'Brien, L.E. (2013). Regional specificity in the Drosophila midgut: setting boundaries with stem cells. Cell Stem Cell *13*, 375–376.

O'Brien, L.E., Zegers, M.M.P., and Mostov, K.E. (2002). Opinion: Building epithelial architecture: insights from three-dimensional culture models. Nat Rev Mol Cell Biol *3*, 531–537.

O'Brien, L.E., Soliman, S.S., Li, X., and Bilder, D. (2011). Altered modes of stem cell division drive adaptive intestinal growth. Cell *147*, 603–614.

Ohlstein, B., and Spradling, A. (2006). The adult Drosophila posterior midgut is maintained by pluripotent stem cells. Nature *439*, 470–474.

Ohlstein, B., and Spradling, A. (2007). Multipotent Drosophila intestinal stem cells specify daughter cell fates by differential Notch signaling. Science *315*, 988–992.

Overeem, A.W., Bryant, D.M., and van IJzendoorn, S.C.D. (2015). Mechanisms of apical–basal axis orientation and epithelial lumen positioning. Trends in Cell Biology *25*, 476–485.

Parslow, A., Cardona, A., and Bryson-Richardson, R.J. (2014). Sample drift correction following 4D confocal time-lapse imaging. J Vis Exp e51086–e51086.

Pellettieri, J., and Alvarado, A.S. (2007). Cell turnover and adult tissue homeostasis: From humans to planarians. Annu Rev Genet *41*, 83–105.

Perdigoto, C.N., Schweisguth, F., and Bardin, A.J. (2011). Distinct levels of Notch activity for commitment and terminal differentiation of stem cells in the adult fly intestine. Development *138*, 4585–4595.

Quan, Z., Sun, P., Lin, G., and Xi, R. (2013). TSC1/2 regulates intestinal stem cell maintenance and lineage differentiation through Rheb–TORC1–S6K but independently of nutritional status or Notch regulation. J Cell Sci *126*, 3884–3892.

Rock, J.R., Onaitis, M.W., Rawlins, E.L., Lu, Y., Clark, C.P., Xue, Y., Randell, S.H., and Hogan, B.L.M. (2009). Basal cells as stem cells of the mouse trachea and human airway epithelium. Proceedings of the National Academy of Sciences *106*, 12771–12775.

Ruiz-Herrero, T., Alessandri, K., Gurchenkov, B.V., Nassoy, P., and Mahadevan, L. (2017). Organ size control via hydraulically gated oscillations. Development *144*, 4422–4427.

Schindelin, J., Arganda-Carreras, I., Frise, E., Kaynig, V., Longair, M., Pietzsch, T., Preibisch, S., Rueden, C., Saalfeld, S., Schmid, B., et al. (2012). Fiji: an open-source platform for biological-image analysis. Nat Methods *9*, 676–682.

Sedzinski, J., Hannezo, E., Tu, F., Biro, M., and Wallingford, J.B. (2016). Emergence of an Apical Epithelial Cell Surface In Vivo. Developmental Cell *36*, 24–35.

Sedzinski, J., Hannezo, E., Tu, F., Biro, M., and Wallingford, J.B. (2017). RhoA regulates actin network dynamics during apical surface emergence in multiciliated epithelial cells. J Cell Sci *130*, 420–428.

Sekiya, K., Futaesaku, Y., and Nakase, Y. (1988). Electron microscopic observations on tracheal epithelia of mice infected with Bordetella bronchiseptica. Microbiol. Immunol. *32*, 461–472.

Sigurbjörnsdóttir, S., Mathew, R., and Leptin, M. (2014). Molecular mechanisms of de novo lumen formation. Nat Rev Mol Cell Biol *15*, 665–676.

Stubbs, J.L., Davidson, L., Keller, R., and Kintner, C. (2006). Radial intercalation of ciliated cells during Xenopus skin development. Development *133*, 2507–2515.

Taniguchi, K., Shao, Y., Townshend, R.F., Cortez, C.L., Harris, C.E., Meshinchi, S., Kalantry, S., Fu, J., O'Shea, K.S., and Gumucio, D.L. (2017). An apicosome initiates self-organizing morphogenesis of human pluripotent stem cells. J Cell Biol *216*, 3981–3990.

Tsujimura, A., Koikawa, Y., Salm, S., Takao, T., Coetzee, S., Moscatelli, D., Shapiro, E., Lepor, H., Sun, T.-T., and Wilson, E.L. (2002). Proximal location of mouse prostate epithelial stem cells : a model of prostatic homeostasis. Journal of Cell Biology *157*, 1257–1265.

Varadarajan, S., Stephenson, R.E., and Miller, A.L. (2019). Multiscale dynamics of tight junction remodeling. J Cell Sci *132*.

Vasquez, C.G., Vachharajani, V.T., Garzon-Coral, C., and Dunn, A.R. (2021). Physical basis for the determination of lumen shape in a simple epithelium. Nature Communications.

Vega-Salas, D.E. (1988). Exocytosis of vacuolar apical compartment (VAC): a cell-cell contact controlled mechanism for the establishment of the apical plasma membrane domain in epithelial cells. The Journal of Cell Biology *107*, 1717–1728.

Viitanen, A., Gullmets, J., Morikka, J., Katajisto, P., Mattila, J., and Hietakangas, V. (2021). An image analysis method for regionally defined cellular phenotyping of the Drosophila midgut. Cell Reports Methods 100059.

Voiculescu, O., Bertocchini, F., Wolpert, L., Keller, R.E., and Stern, C.D. (2007). The amniote primitive streak is defined by epithelial cell intercalation before gastrulation. Nature *449*, 1049–1052.

Walck-Shannon, E., and Hardin, J. (2014). Cell intercalation from top to bottom. Nat Rev Mol Cell Biol *15*, 34–48.

Wang, A.Z., Ojakian, G.K., and Nelson, W.J. (1990). Steps in the morphogenesis of a polarized epithelium. I. Uncoupling the roles of cell-cell and cell-substratum contact in establishing plasma membrane polarity in multicellular epithelial (MDCK) cysts. Journal of Cell Science *95 (Pt 1)*, 137–151.

Xiang, J., Bandura, J., Zhang, P., Jin, Y., Reuter, H., and Edgar, B.A. (2017). EGFR-dependent TOR-independent endocycles support Drosophila gut epithelial regeneration. Nat Commun *8*, 15125.

Xu, C., Tang, H.-W., Hung, R.-J., Hu, Y., Ni, X., Housden, B.E., and Perrimon, N. (2019). The Septate Junction Protein Tsp2A Restricts Intestinal Stem Cell Activity via Endocytic Regulation of aPKC and Hippo Signaling. Cell Rep *26*, 670-688.e6.

Yanagihashi, Y., Usui, T., Izumi, Y., Yonemura, S., Sumida, M., Tsukita, S., Uemura, T., and Furuse, M. (2012). A novel smooth septate junction-associated membrane protein, Snakeskin, is required for intestinal barrier function in Drosophila. Journal of Cell Science *125*, 1980–1990.

Yang, Q., Xue, S.-L., Chan, C.J., Rempfler, M., Vischi, D., Maurer-Gutierrez, F., Hiiragi, T., Hannezo, E., and Liberali, P. (2021). Cell fate coordinates mechano-osmotic forces in intestinal crypt formation. Nat Cell Biol *23*, 733–744.

Yu, H.H., and Zallen, J.A. (2020). Abl and Canoe/Afadin mediate mechanotransduction at tricellular junctions. Science *370*.

Moreno-Roman_Fig1

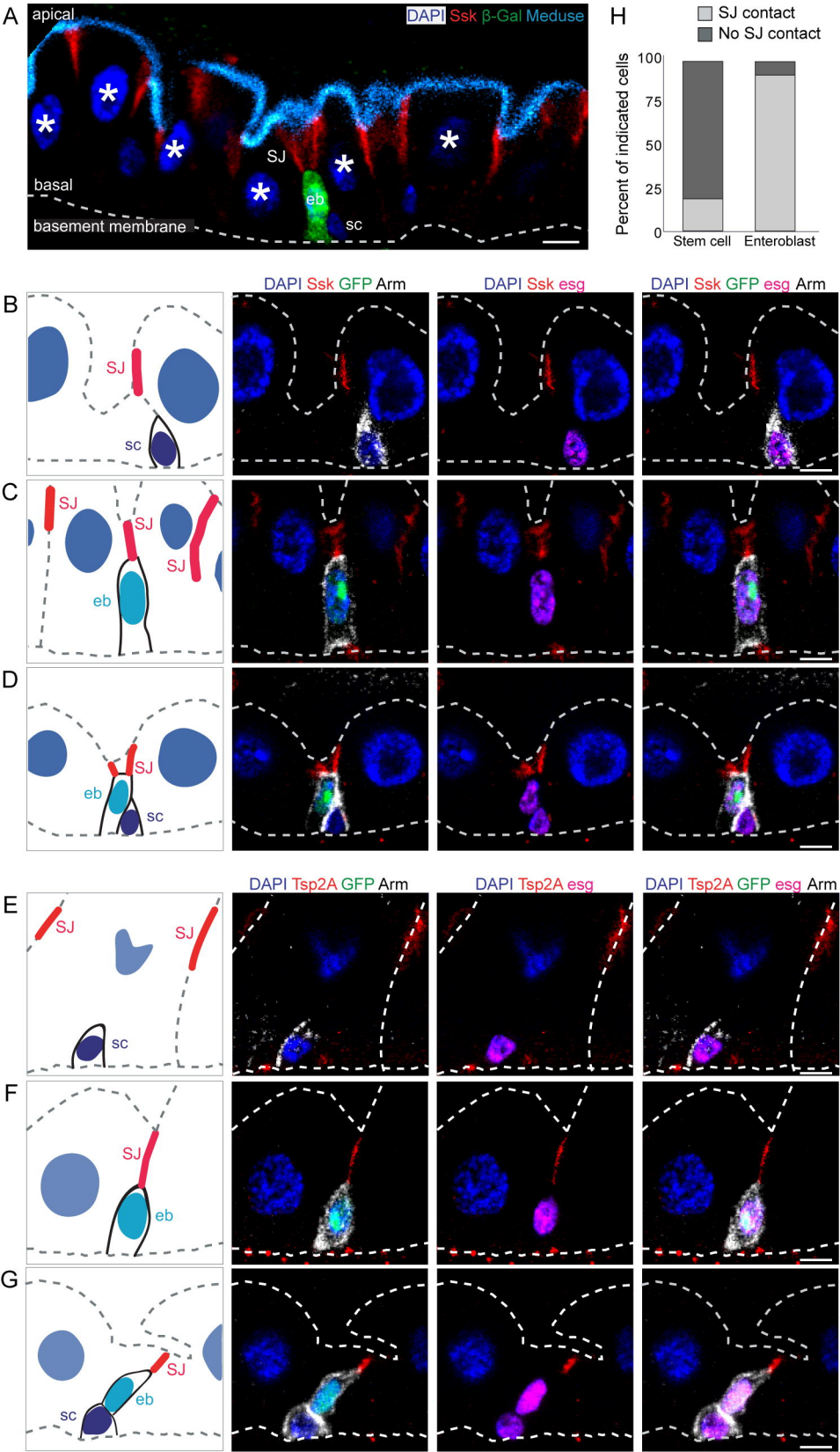

Moreno-Roman_Fig2

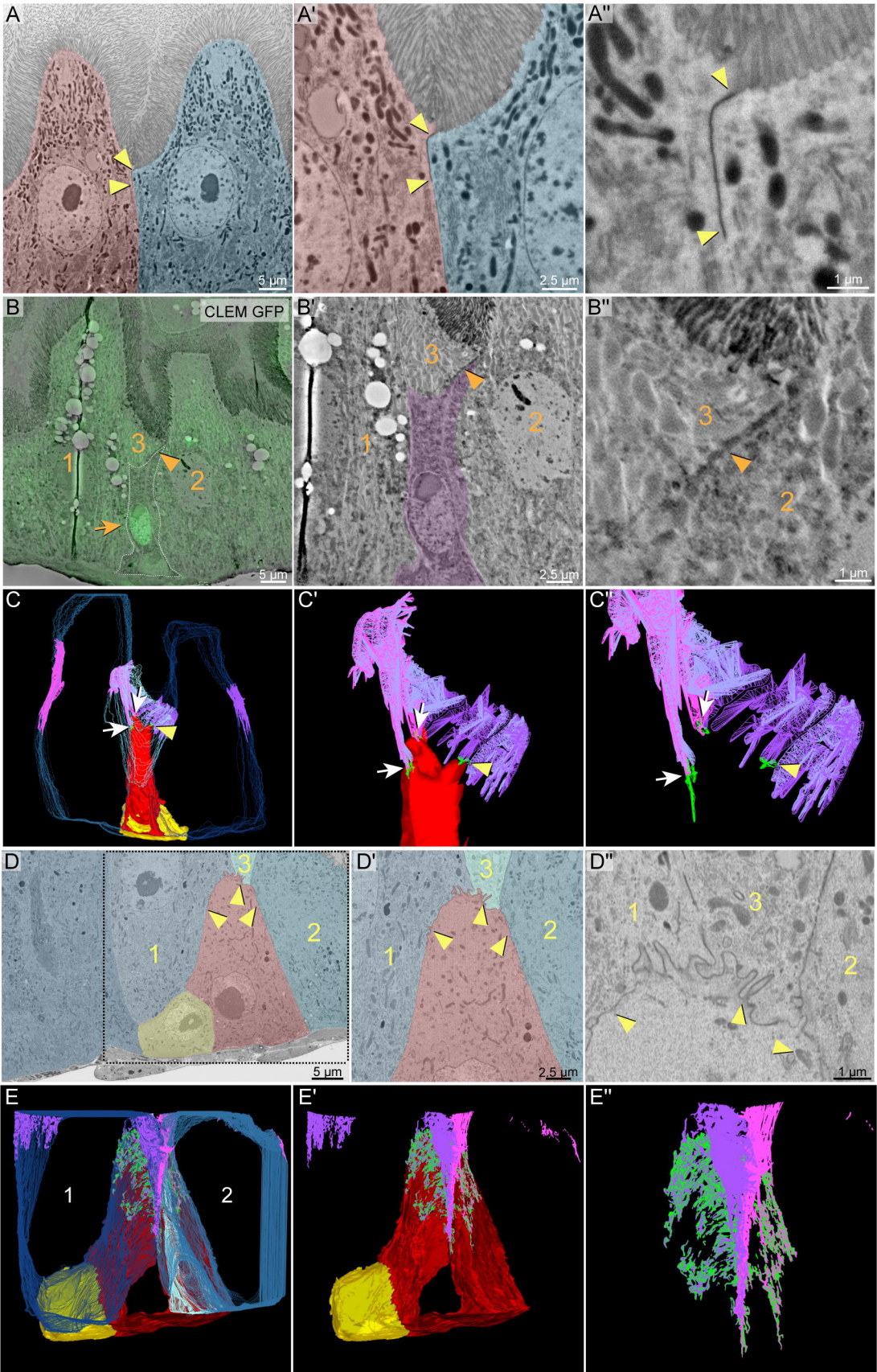

Moreno-Roman_Fig3

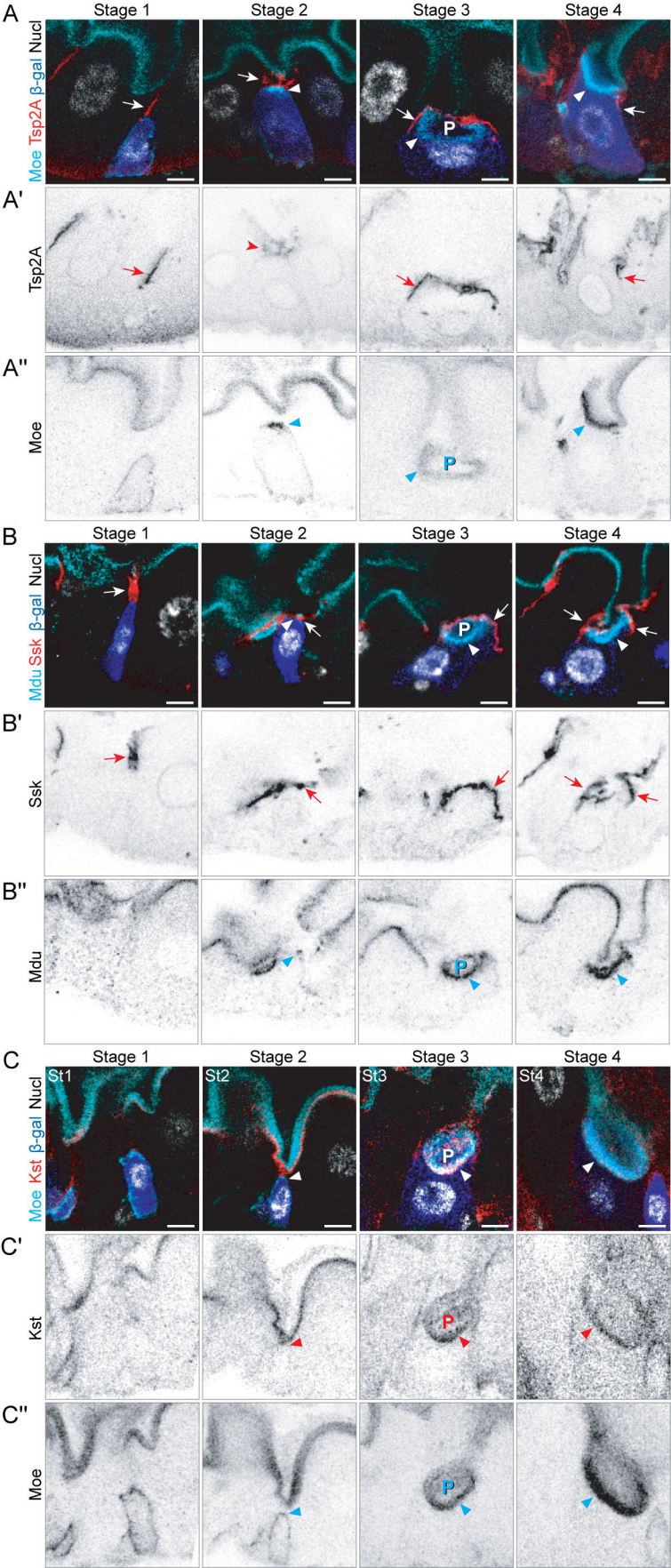

Moreno-Roman_Fig 4.

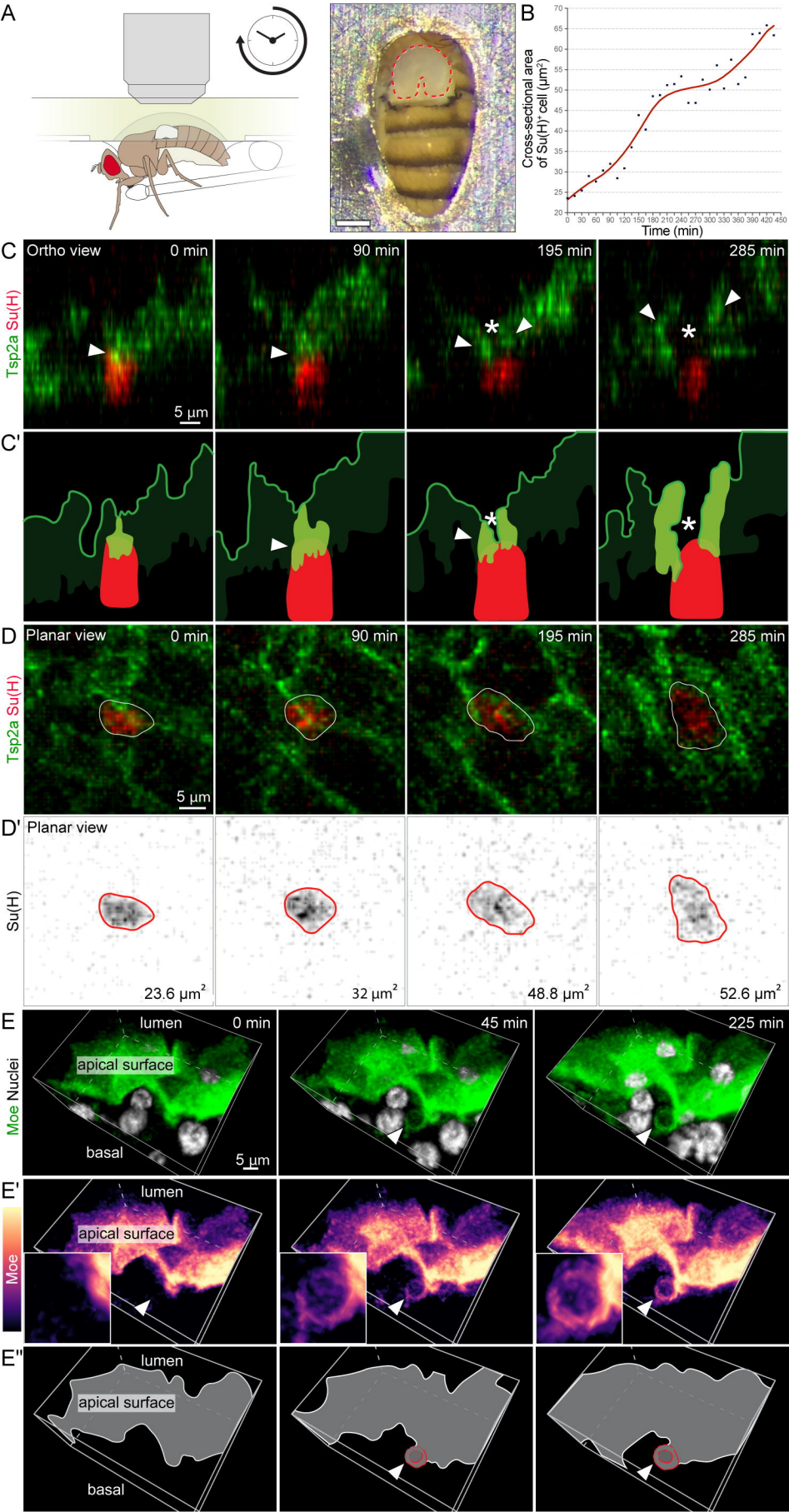

Moreno-Roman_Fig 5

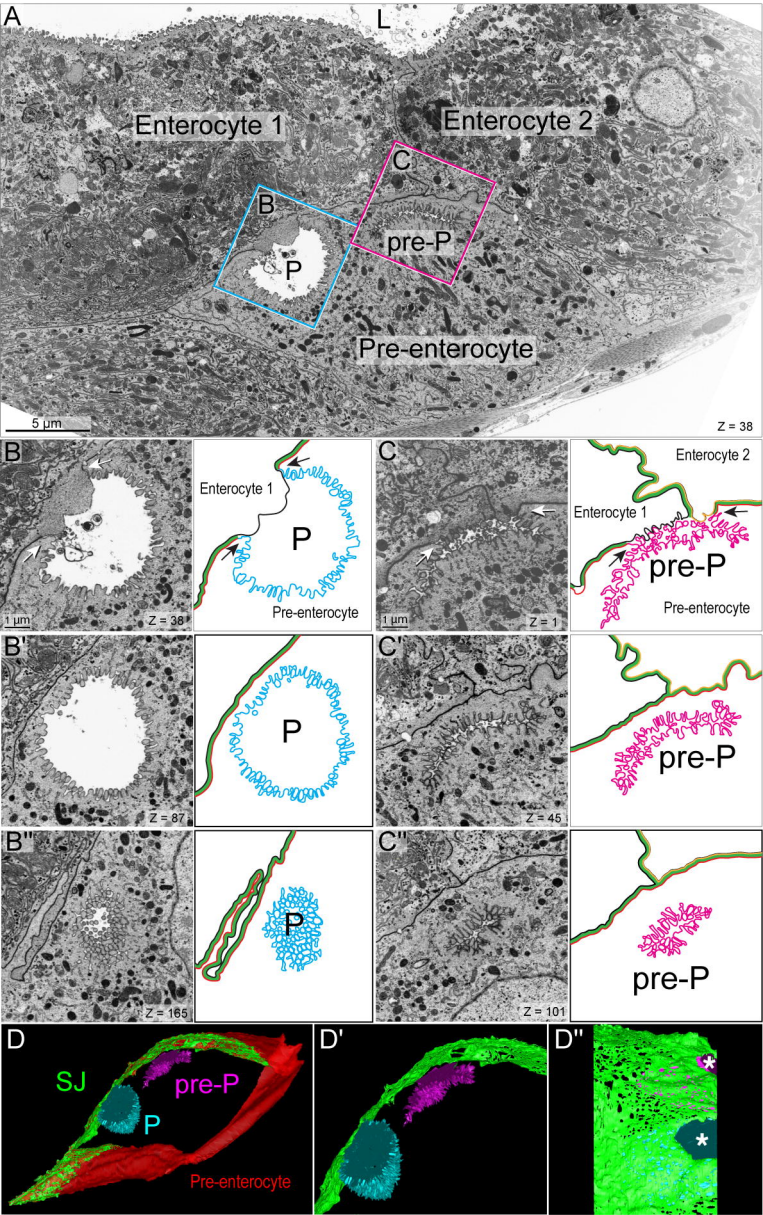

Moreno-Roman_Fig 6

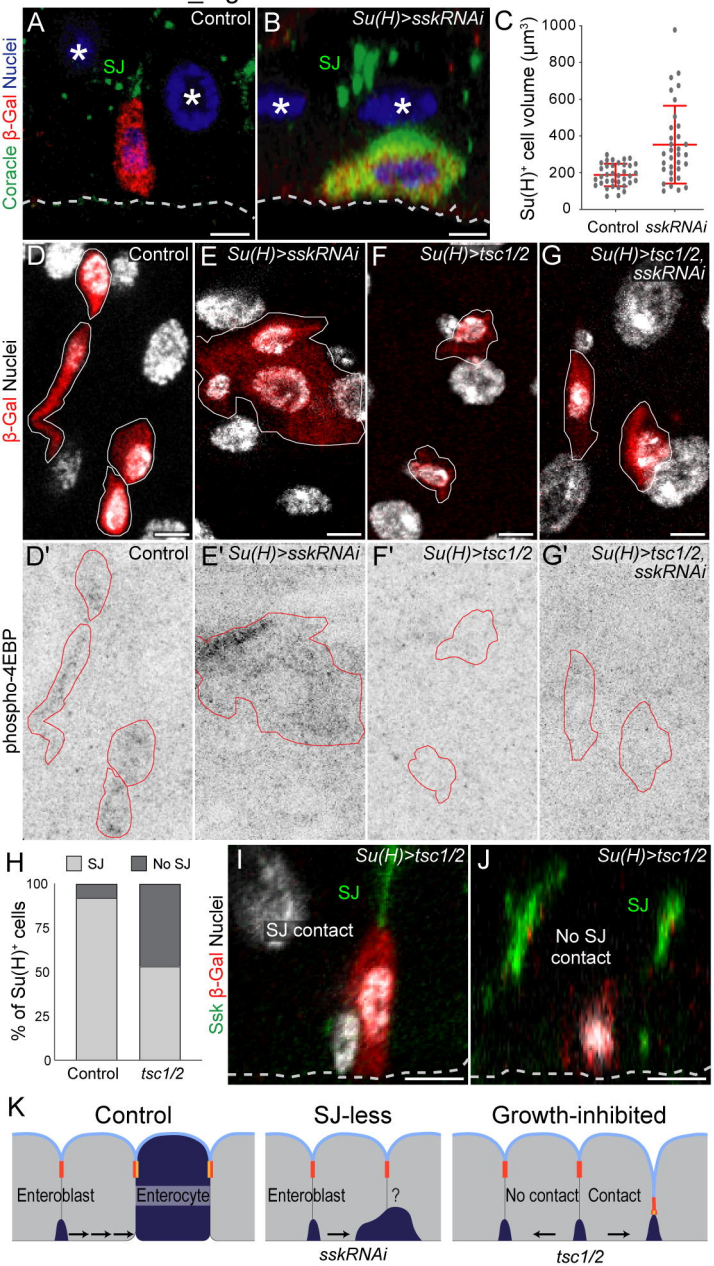
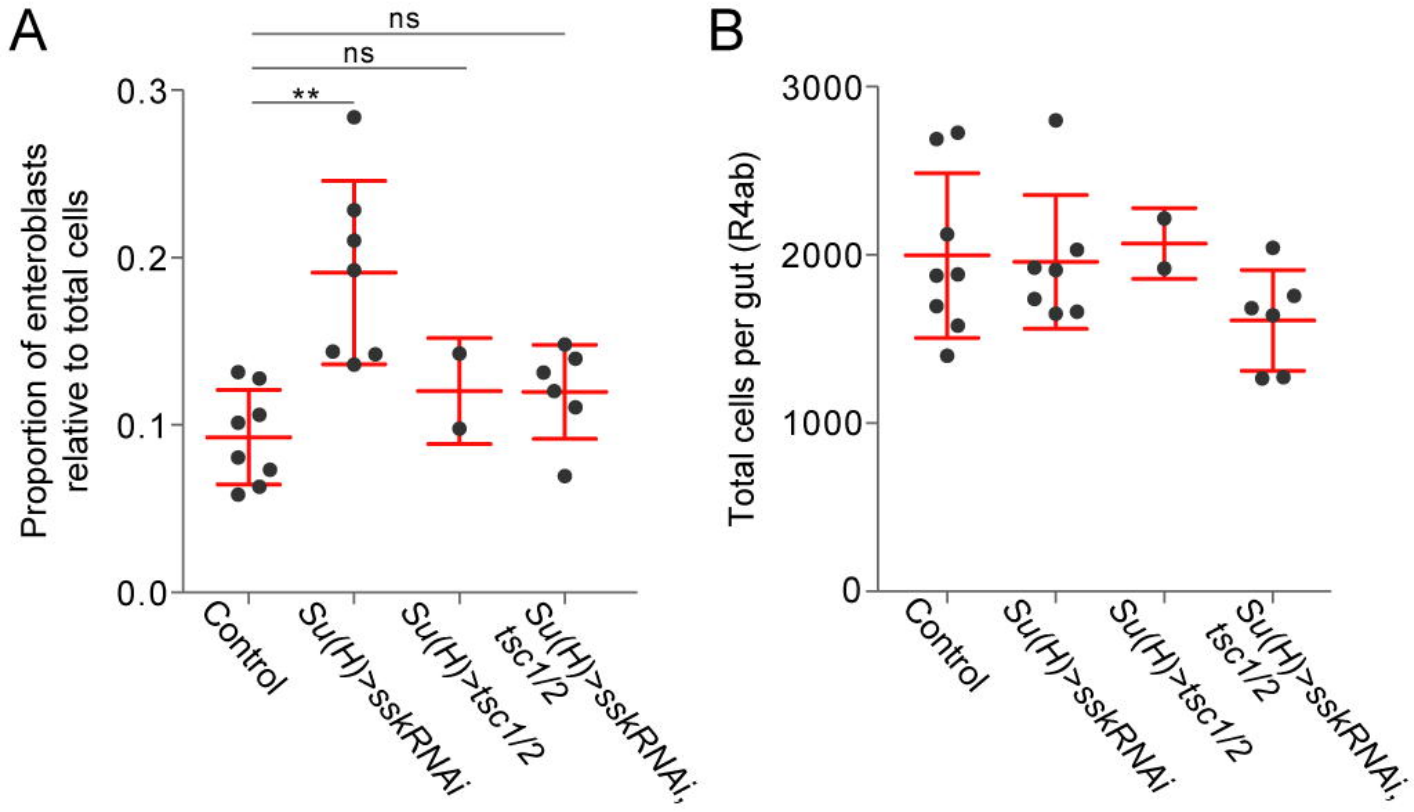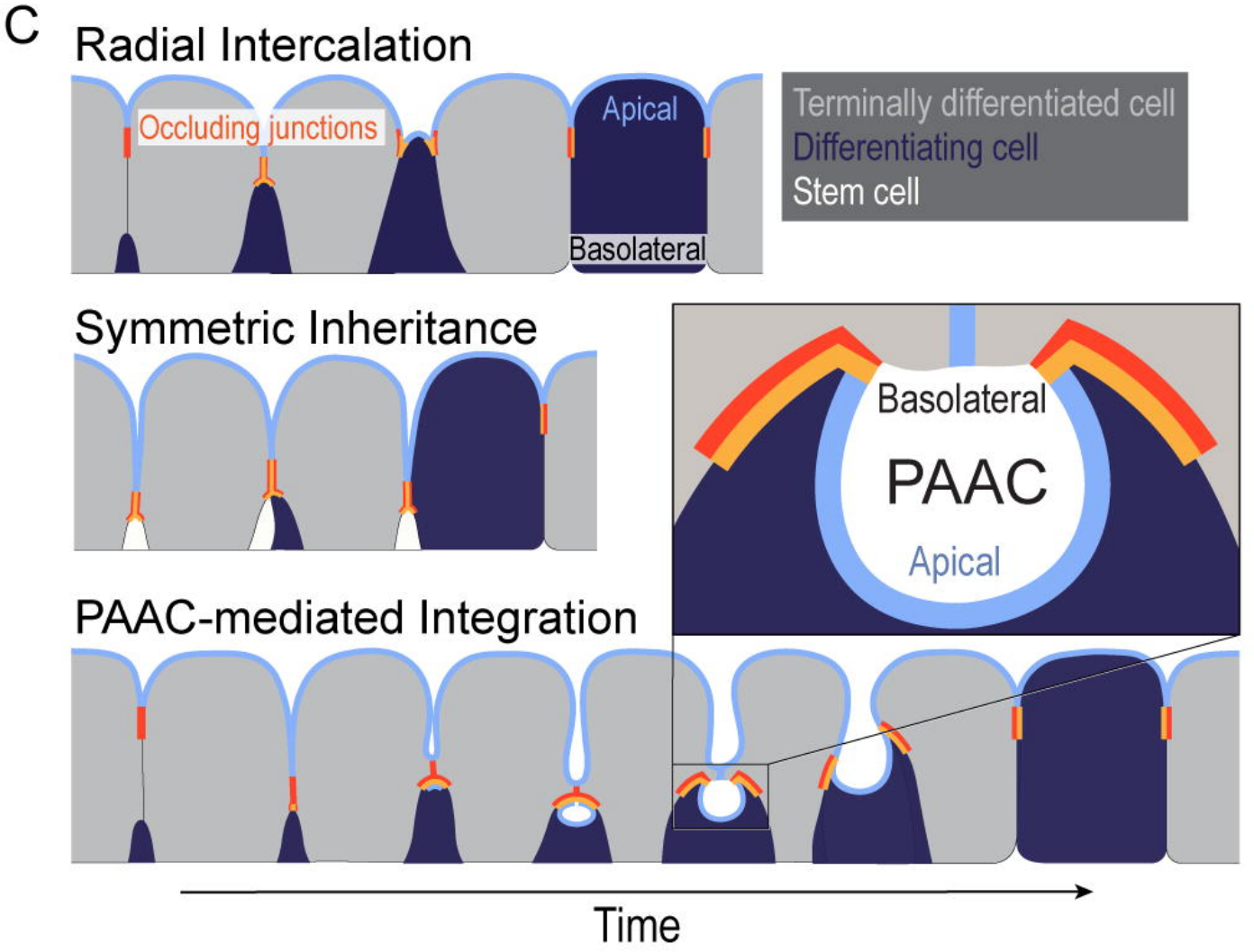
Moreno-Roman_Fig 7